

Review

Ferroelectric Materials: A Novel Pathway for Efficient Solar Water Splitting

Sangmo Kim, Nguyen Thi Nguyen and Chung Wung Bark * 

Department of Electrical Engineering, Gachon University, Seongnam 13120, Korea; singmul0227@gmail.com (S.K.); ngtnghuyen1710@gmail.com (N.T.N.)

* Correspondence: bark@gachon.ac.kr; Tel.: +82-31-750-5351

Received: 27 July 2018; Accepted: 25 August 2018; Published: 1 September 2018



Abstract: Over the past few decades, solar water splitting has evolved into one of the most promising techniques for harvesting hydrogen using solar energy. Despite the high potential of this process for hydrogen production, many research groups have encountered significant challenges in the quest to achieve a high solar-to-hydrogen conversion efficiency. Recently, ferroelectric materials have attracted much attention as promising candidate materials for water splitting. These materials are among the best candidates for achieving water oxidation using solar energy. Moreover, their characteristics are changeable by atom substitute doping or the fabrication of a new complex structure. In this review, we describe solar water splitting technology via the solar-to-hydrogen conversion process. We will examine the challenges associated with this technology whereby ferroelectric materials are exploited to achieve a high solar-to-hydrogen conversion efficiency.

Keywords: water splitting; ferroelectrics; hydrogen production; solar energy

1. Introduction

In order to effectively address energy-related problems such as global warming, which is caused by the emissions of air pollutants including carbon dioxide (CO₂), there is a growing interest in many kinds of renewable energy (such as solar, wind power, hydroelectric energy, and biomass), and their related applications as an alternative to fossil fuels [1,2].

Among the various alternative energy sources, solar energy is an almost unlimited and clean energy source, given that the Sun has been providing energy in the form of light and heat to the Earth for more than four billion years. Until now, solar energy has been considered as an alternative energy option that could help address several problems of global importance such as an insufficient energy supply, environmental pollution, and fossil fuel resource depletion. Moreover, most regions of our planet including the atmosphere, oceans, and soil receive approximately 3850 zetta joules (ZJ = 10²¹ J) of energy every year (~0.539 ZJ of energy was consumed worldwide in 2010). Considering only the amount of energy received from the Sun, solar energy is one of best candidates as a substitution for fossil fuels. Even though many researchers have been actively involved in alternative energy research and related technologies have been developed over the years, no more than 1% of the energy produced by the Sun is used by our planet. Therefore, we need to concentrate on the efficiency of solar energy use, whether indirectly or directly [3,4]. In particular, for a solar energy carrier, three main points have to be considered. (1) How much cheaper and abundant are chemical reactants? (2) Is the carrier easily stored and transported? (3) In the process, is carbon dioxide generated and emitted?

On the other hand, hydrogen energy and related applications are considered to be excellent alternative renewable energy carriers due to their storability, transportability, and convertibility to energy on demand. Hydrogen gas is a clean, nontoxic, colorless, and eco-friendly source (does not release carbon dioxide) that could be obtained by splitting naturally occurring water into hydrogen

and oxygen. Moreover, hydrogen could be used in various energy applications such as hydrogen fuel cells (HFCs), combustible fuel, and synthetic natural materials. It is known that when the gas is used for electricity production such as in the case of hydrogen-powered fuel cells, it has three times the efficiency of electricity generation (~65%) compared to conventional combustion-based power plants (~35%) [5–7].

In order for hydrogen to be classified as an environmentally friendly alternative energy source, it should be produced using appropriate processes that use carbon-free environmentally friendly materials instead of fossil fuels. Compared with other methods of hydrogen production (biomass, thermal decomposition of natural gas, water electrolysis, and thermochemical cycles), water-splitting technology has been proposed as the most suitable method for the eco-friendly generation of hydrogen gas from water. It should be noted that solar energy has been used as an energy conversion source of solar thermal and photovoltaics starting from solar light. In particular, water splitting using photovoltaics based on solar energy is ideal for the generation of hydrogen gas from water [8,9].

This review will address solar water-splitting technology (such as water splitting in photosynthesis, photoelectrochemical water splitting, and photocatalytic water splitting), including the systems involved and hydrogen production from water and solar energy. Moreover, we will introduce the recent progress in solar water splitting using ferroelectric materials, and summarize how each material plays an important role in achieving efficient solar water splitting.

2. Overview of Solar Water Splitting

In a solar water-splitting system, hydrogen is produced from the semiconductor–electrolyte interface where sunlight is absorbed in the depletion layer and electron–hole pairs are separated to drive the chemical reaction at the semiconductor–electrolyte interface. Light energy is used to directly dissociate water molecules into hydrogen and oxygen through the following steps: light absorbance, conversion of light to exciton (electron–hole pair), and chemical reaction (separated hydrogen). Water splitting via solar energy is achieved through three kinds of hydrogen production systems [8–12]: (1) particulate photocatalysis (PC) systems, (2) photoelectrochemical (PEC) systems, and (3) photovoltaic–photoelectrochemical (PV–PEC) systems, as shown in Figure 1. In this section, we describe in more detail the mechanism for solar energy conversion to hydrogen fuel, and the as-mentioned three approaches for hydrogen generation are introduced.

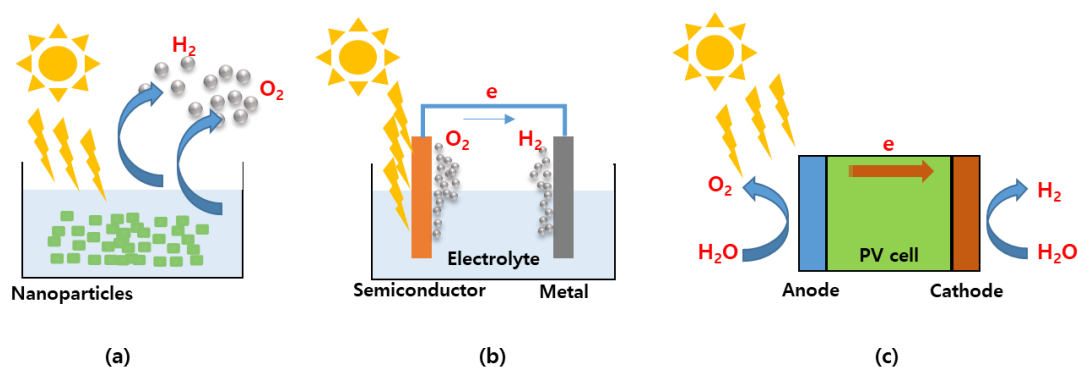


Figure 1. The solutions for solar hydrogen via water splitting. (a) Particulate photocatalytic (PC) water splitting system, (b) Photoelectrochemical (PEC) water splitting system and (c) Photovoltaic–photoelectrochemical hybrid (PV–PEC) system [10]. Copyright 2017, Elsevier.

2.1. Basic Mechanism for Solar Energy to Hydrogen Conversion System

The concept of photocatalytic water splitting (PWS) was introduced by hydrogen production via photoelectrochemical water splitting with a rutile TiO_2 (anode) as the photocatalyst, and a platinum

(cathode). This was first reported by Fujishima and Honda in 1972 [13]. Hydrogen could be generated directly from water, and solar light could be generated through the solar energy conversion process.

In PWS systems, photocatalysts play an important role in the conversion of solar energy to hydrogen in response to visible light in the water-splitting system. The hydrogen gas production process involves a photocatalytic reaction such as the direct conversion of solar energy into hydrogen gas in a semiconductor with an energy bandgap that is positioned between their energy band structures.

A photocatalytic water-splitting reaction via semiconductor-based photocatalysts is conducted in terms of charge carrier generation, separation, transport, and transfer. This refers to the following three-step process [10–14].

Step 1: Light (photons) is absorbed near the surface of the semiconducting materials with energies greater than their bandgap energy (e.g., ~1.7 eV). Excited electrons (excitons) and holes are generated inside the semiconducting materials by bandgap excitation.

Step 2: The electrons and holes henceforth referred to as photogenerated electrons and holes are separated in the bandgap and drift to the surface of the semiconducting materials, causing the release of oxygen from water (catalytic water oxidation reaction).

Step 3: The photogenerated electrons combine with H⁺ via the metal electrode (catalytic water reduction reaction).

Figure 2 shows the principle of photocatalytic water-splitting reactions with photoelectrons and holes that are generated by the absorption of light. The photoelectrons and holes reduce and oxidize water on the surface of the semiconductors as the two half-reactions of water splitting via the following reactions [10–12].

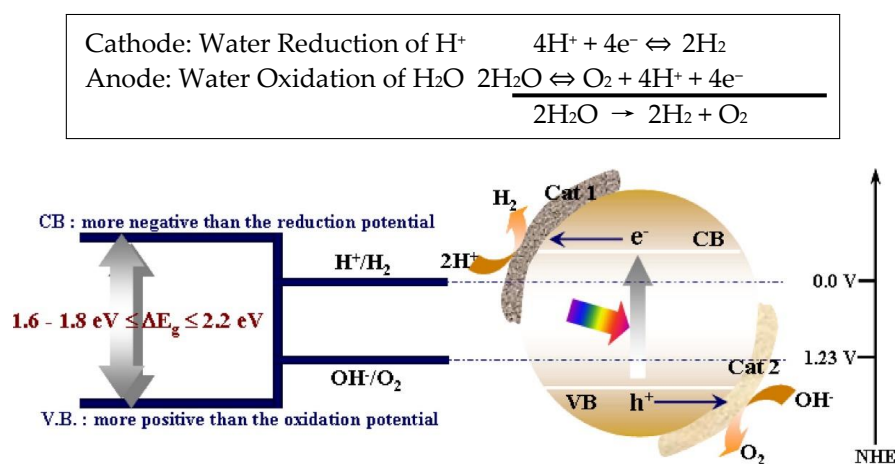


Figure 2. Principle of photocatalytic water-splitting (PC) reactions [7]. Copyright 2014, Elsevier.

The water-splitting reaction is thermodynamically nonspontaneous, and therefore is an uphill reaction. As such, the net Gibbs free energy ($\Delta G \approx 237 \text{ kJ/mol}$) needs to be increased. Namely, if a photocatalyst has a bandgap that is larger than the energy required for water splitting (~1.23 eV), then its conduction and valence band edge should contain the oxidation and reduction potential of water [8].

It is clear that the O₂/H₂O redox potential difference is 1.23 V. Therefore, the requirement of a bandgap is larger than the required energy for water splitting (1.23 eV). For more details, the valence band potential must be more positive than the O₂/H₂O redox potential of 1.23 V versus Normal hydrogen electrode (NHE, pH = 0) to permit water oxidation, and the conduction band must be more negative than the H⁺/H₂ redox potential of 0 V versus NHE to facilitate water reduction [8–10].

2.2. Solar Energy to Hydrogen Conversion System for Solar Water Splitting

Among the previously mentioned hydrogen production systems, i.e., the PC, PEC, and PV-PEC, the PC offers reasonable solar-to-hydrogen efficiency, a low process cost, simplicity of design, and a large-scale method for water splitting. Moreover, the PC reaction could be performed in the homogeneous phase without transparent electrodes and directional illumination. However, a PC system should be inserted in a gas separator because both hydrogen and oxygen gases are produced during the water-splitting process. Therefore, an enclosed reaction system is required on a large-scale [10,14–16]. However, the PEC systems do not require gas separation due to their structure, which entails one or two conductive electrodes and a small bias. The two different gases are sequentially generated and remain at the opposite electrodes.

A PEC cell system is composed of an electrolyte, an n-type semiconductor (anode), and a p-type semiconductor (cathode) with a semiconductor/liquid junction, as shown in Figure 3. Photogenerated charge carriers are separated, and minor carriers (holes and electrons originated from p-/n-type semiconductor electrodes) move within the semiconductor–liquid interface. This allows for the separate release of oxygen and hydrogen gases during the water-splitting reaction.

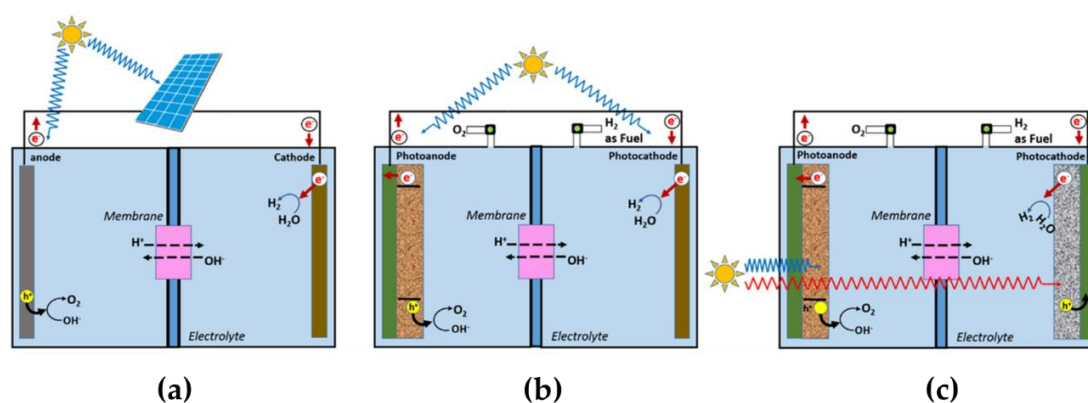


Figure 3. Schematic diagram of photoelectrochemical (PEC) photovoltaic (PV)-PEC hybrid water splitting system; (a) PV/PEC hybrid cell, (b) A photoelectrode PEC cell with anode and cathode combined in parallel, and (c) Two photoelectrodes combined in series [3]. Copyright 2010, Royal Society of Chemistry.

In electrode–liquid electrolyte systems, the photovoltaic and photoelectrochemical reaction behavior is mainly conducted in three steps: (1) light absorption, (2) water reduction and oxidation, and (3) the recombination of electrons and holes. When the system is exposed to photons with sufficiently high light energy, they are induced to form electron–hole pairs, resulting in chemical reactions such as oxidation–reduction reactions. During these reactions, photogenerated currents and voltages are observed inside the system. Such electrical phenomena can be observed in both photovoltaic and photoelectrochemical systems. The photovoltaic (PV) process is so-called because the conversion of light into electricity occurs in a photoelectrode through a process of conversion photons. In the case of a photoelectrochemical process, the generated photons induce a chemical reaction in the electrodes. Since both photovoltaic and photoelectrochemical processes are related to light absorbance and the conversion of photons to induce chemicals reactions, various semiconducting materials can be used to convert solar energy to hydrogen. They have been extensively used in the past for solar water splitting [17,18].

Until now, several different concepts have been proposed and reported from different research groups for solar water splitting. Figure 3 shows a schematic diagram of an enhanced PEC and PV-PEC hybrid water splitting system, which was proposed to improve solar energy to hydrogen efficiency. The PV/PEC hybrid cell consists of a photoelectrode PEC cell and a PV cell. The PV cells play an important role in supplying a potential to the PV cell. The PV cell assists the PEC cell

to develop a potential for photogenerated electrons, allowing water reduction at the surface of the photocathode [19,20].

2.3. Strategy for High Solar-to-Hydrogen (STH) Efficiencies

The energy conversion efficiency in solar water-splitting cells is usually evaluated by various methods such as standard solar-to-hydrogen (STH) conversion efficiency (η_{STH}), quantum efficiencies such as the incident photon-to-current efficiency (IPCE), photon-to-current efficiency (ABPE), and the absorbed photon-to-current conversion efficiency (APCE) [21,22]. Among these, we will further examine the standard η_{STH} and ABPE in greater detail.

The standard η_{STH} is the ratio between the total energy generated and the total energy input in the sunlight irradiation of AM 1.5 G (air mass at a solar zenith angle of 48.2°), which can be calculated using following the equation:

$$\eta_{STH} = \frac{\text{Total Energy generated}}{\text{Total energy input}} = \frac{\Delta G \times r_{H_2}}{P_{sun} \times S} \quad (1)$$

where ΔG is the Gibbs free energy (237 kJ/mol), r_H is the rate of hydrogen production in moles per second, P_{sun} is the incident light intensity (100 mW/cm²) and S is the illuminated area of the photoelectrode (cm²).

The ABPE can be calculated from the J–V curve of the photoelectrode while an external bias is applied to the two electrodes.

$$\text{ABPE (\%)} = \left[\frac{J \text{ (mA/cm}^2\text{)} \times (1.23 - V_{bias} \text{ (V)})}{P_{in} \text{ (mA/cm}^2\text{)}} \right]_{AM 1.5G} \times 100 \% \quad (2)$$

2.4. Strategy to Improve High STH Efficiency for Water Splitting

Solar water splitting with high STH efficiencies has been developed over the last few years. Recently, Jia et al. [23] reported on solar water splitting by photovoltaic–electrolysis STH with an efficiency over 30% for two days using two polymer electrolyte membrane electrolyzers in series with one InGaP/GaAs/GaInNAs(Sb) triple junction solar cell.

To achieve high STH efficiency for solar water splitting, we should carefully select the semiconducting materials. The bandgap of the semiconducting materials, including the electrode, is very important in the solar water-splitting process. Most photons cannot be absorbed by the semiconductor if they have energy that is lower than the bandgap energy. Therefore, the bandgap of the selected semiconducting materials must be chosen in the range of at least ~1.23–2.0 eV to absorb light in the visible range, which facilitates a high photocatalytic effect. The semiconducting materials used for the cells should have strong catalytic activity and stability regardless of the oxidation/reduction reaction. With regard to the process, the semiconductor is easily oxidized and reduced by excited electrons and holes. Since their photoreproductive capability decreases, the cell's STH efficiency also decreases. Additionally, the materials used for cells should be easily modified and readily available at low cost [23–25].

3. Solar Energy Conversion of Ferroelectric Materials

3.1. Ferroelectric Effect and Materials

The basic concept of ferroelectricity was introduced by Rochelle salt in 1920: if an external electric field is applied to a ferroelectric material, the dipoles in the crystalline or polycrystalline structure are induced to produce a ferroelectric phenomenon with spontaneous polarization and alignment with the external field. Even when the electric field is switched off, the material maintains a spontaneous polarization. This is called the ferroelectric phenomenon. Furthermore, the spontaneous polarization is reversed by the application of an electric field. Ferroelectrics exhibit a phase transition phenomenon.

Namely, the polarization of the dipoles exhibits interactive electric dipole moments with and without an applied electric field. When the ferroelectric is at a higher temperature than the phase transition temperature, the spontaneous polarization is lost due to thermal fluctuations.

When the spontaneous polarization is reversed, it causes the ferroelectrics to exhibit the property of piezoelectricity. Ferroelectric materials can be categorized into two types: the order–disorder type and the displacement type, based on the physical mechanism used to generate the ferroelectric characteristics.

Ferroelectric materials, which are mostly used as condenser and as semiconductor elements, are a cubic system with a perovskite structure. When the crystal structure of the perovskite exceeds the Curie temperature T_c (~ 120 °C), similar to a ferroelectric crystal of the ABO_3 perovskite structure, it changes its form to a paraelectric phase in which the crystal structure is the cubic symmetry [26,27].

3.2. Ferroelectric Photovoltaics—Phenomenology of Ferroelectric Solar Cells

The photovoltaic effect in a semiconducting material occurs when an asymmetry in the electric potential occurs throughout the materials due to a flow of photogenerated electrons and holes. A photocurrent occurs as a result of the absorption of photons with high energy, which leads to the transfer of electrons from the valence band (VB) to the conduction band (CB).

Conventional photovoltaic phenomenon could be observed in interfaced doped semiconductors such the p–n junction structure when the following three processes should be involved: high light absorption, generation of the electron–hole pairs, and separation of the free charges.

Usually, hole (positive charge) and electron (negative charge) carriers are generated by high energy photons. Over time, the excited carriers return to the ground-state level, and the internally absorbed energies are released as light or heat. While most commercial solar cells are based on the p–n junction principle between two different metallic contacts, they are limited by the so-called Shockley–Queisser limit, which prevents any single p–n junction solar cell from converting more than 33.7% of the incident light [23]. Their heterojunction structure is limited with regard to the selection of potential materials due to dopant issues and the mismatched lattice of the structure.

Ferroelectric materials have been recently proposed as excellent potential candidates to solve these problems. The phenomenon of a photovoltaic effect in a ferroelectric has been observed in $BaTiO_3$, $LiNbO_3$, and $Pb(Zr,Ti)O_3$ with weak pyroelectric currents (photovoltaic current above T_c). However, ferroelectrics have a significant disadvantage of large band gaps in the range of ~ 3 – 4 eV, which is challenging for applications as photovoltaic materials. Their large band gaps values result in the degradation of efficient conversion because small current densities and large open circuit photovoltages are typical. In recent years, the higher efficiency of narrower bandgap ferroelectrics in ferroelectric solar cells such as those of $BiFeO_3$ (BFO, 2.2–2.7 eV) and multiferroic $Bi_{12}FeCrO_6$ (BFCO, 1.9–2.1 eV), has been reported.

Ferroelectric photovoltaic effects are divided into photoferroic phenomena including the bulk photovoltaic effect (BPE) and the anomalous photovoltaic effect (APE). Photoferroic phenomena could be demonstrated in hybrid organic–inorganic halide perovskites such as $CH_3NH_3PbI_3$ (MAPI) to fabricate high-efficiency photovoltaic devices. Ferroelectric domains as internal junctions can induce the generation of photoexcited electrons and hole pairs, and decrease recombination by dividing charged carriers. The effect could produce a higher open circuit voltage (V_{OC}) and the current–voltage hysteresis observed in perovskite solar cells. The photoferroic system has an intricate interface between the photoresponse and the ferroelectric phase stability, single/multidomain, and distributions. The photoferroic system has recently achieved power efficacies in excess of 8% power for Bi_2FeCrO_6 [26]. The larger bandgap (~ 3 eV) in the polar materials shows their potential for development as light absorbers [25–27].

The photovoltaic effect (BPE) is a phenomenon that is observed in an open circuit voltage under dark illumination. The BPE generates a photovoltaic current that results in an anomalous photovoltaic effect (APE), as a type of bulk photovoltaic effect that occurs between semiconductors and insulators

as a result of an open-circuit voltage induced by light. Sometimes, the generated voltage approaches almost thousands of volts.

The mechanisms of the anomalous photovoltaic effect (APE) are schematically represented in Figure 4. The generated photovoltage in the anomalous photovoltaic effect (APE) is limited by its bandgap. This results in a photoresponse of the heterojunctions, the photo-Dember effect, and grain boundaries. As shown in Figure 4, its mechanisms could be explained by three categories as follows: (a) the photo-Dember effect, (b) p–n homojunction domains, (c) and ferroelectric domains [27,28].

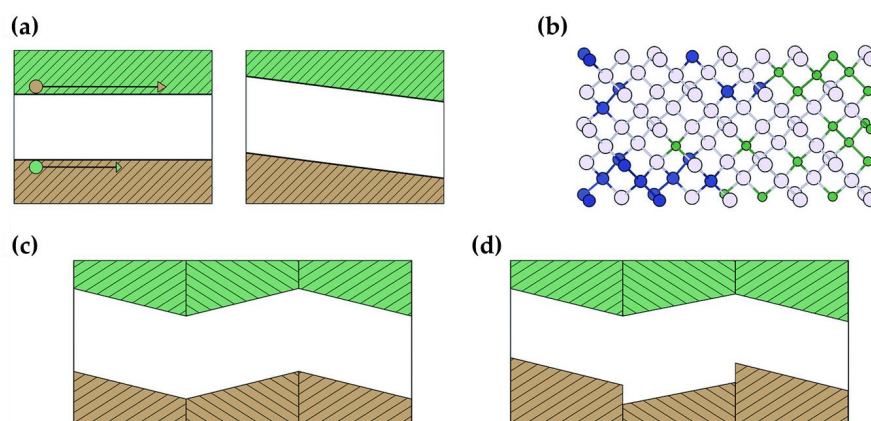


Figure 4. Conventional models for the polycrystalline anomalous photovoltaic effect [27]. Copyright 2015, Royal Society of Chemistry.

4. Ferroelectric Materials for Photoelectrochemical (PEC) Water-Splitting Devices

4.1. General Requirements for Photoelectrode Materials

The choice of appropriate materials for photoelectrodes plays a decisive role in the PEC activity for water splitting. Conventional materials, including semiconductors, can be categorized into wide-bandgap and narrow band-gap materials. Traditionally, wide-bandgap materials (TiO_2 , SrTiO_3 , BaTiO_3 , and WO_3) are considerably stable in an electrolyte solution, but they can have the limited absorbance range in the ultraviolet region. Even though narrow bandgap materials (Cu_2O , InAs , and CuO) can absorb much more visible light irradiation in the solar spectrum, they have a high possibility of being damaged from strong electrolytic environments. However, we do not have many options for selecting suitable materials for photoelectrodes (photocathodes and photoanodes) of PEC. For photocatalytic water splitting, the selected materials must have bandgaps of approximately 2 eV (at least 1.23 eV) as a result of thermodynamic energy and kinetic loss. Figure 5 shows the bandgap of various materials. Therefore, it is imperative that the following general requirements are met prior to the fabrication of high-performance PECs [12,29,30].

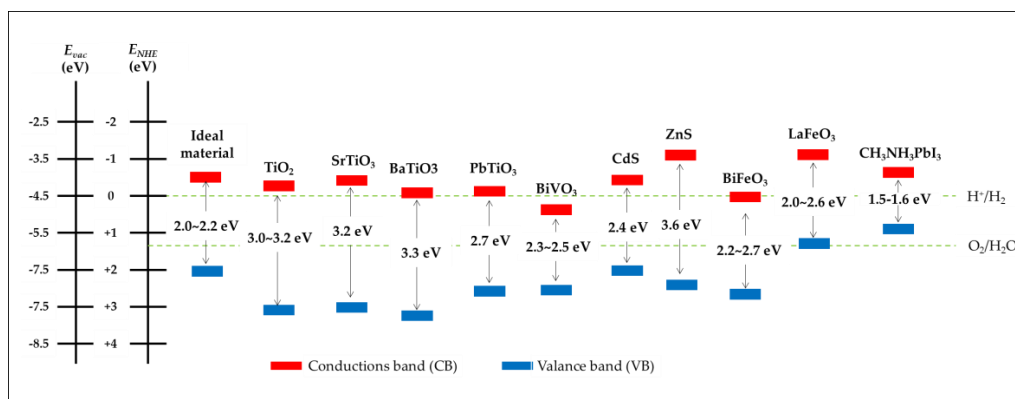


Figure 5. The bandgap of various materials including ferroelectrics and the semiconductor.

(i) Suitable bandgap energy and band edge positions. The electrolysis of water is composed of two reactions occurring at different electrodes. There is a reduction reaction generating hydrogen with H^+/H_2 redox potential of 0 V vs. NHE at the photocathode, whilst the $\text{O}_2/\text{H}_2\text{O}$ redox potential of 1.23 V vs. NHE (pH = 0) in an oxidation reaction at the photoanode; thus, the bandgap of the materials needs to be larger than 1.23 V in order to be able to occur water split. In addition, the thermodynamic energy losses (0.3–0.4 V) and an overpotential (0.4–0.6 V) should also be considered. Consequently, a minimum bandgap of ~1.8 eV is required. Furthermore, visible light is very limited below 390 nm, and this limits the upper value of the bandgap energy to 3.2 eV. Therefore, materials with a bandgap energy in the range between 1.9–3.2 eV are promising candidates for the generation of large photovoltages. When a photoelectrode material that meets these requirements with respect to the bandgap value absorbs incoming photons, electrons are excited to the conduction band (CB) and leave holes in the valence band (VB). The CB edge must be more negative than the H^+/H_2 redox potential of 0 V versus normal hydrogen electrodes (NHEs) (pH = 0) to induce H_2 production, while the VB edge value must be more positive than the $\text{O}_2/\text{H}_2\text{O}$ redox potential of 1.23 V versus NHE to generate water oxidation.

(ii) Efficient charge separation and transfer. Low efficiency in PEC devices is mostly attributed to charge recombination and inefficient carrier transportation. As a result, many studies have been performed with the objective of addressing these challenges to achieve enhanced performance on PEC devices. Both the intrinsic properties (hole and electron mobility) and the extrinsic properties (crystallinity, nanostructure) affect the separation and transfer of the photogenerated carriers.

(iii) Robust catalytic activity and stability. Generally, there are energy barriers for the transfer of electrons or holes, and these barriers exhibit energy losses in the reaction. Appropriately rapid surface reaction kinetics can overcome these barriers and suppress electron–hole recombination. In PEC systems, the hydrogen evolution reaction (HER) generates H_2 from H^+ (in acid) or H_2O (in base), whereas oxygen evolution reaction produces O_2 from H_2O (in acidic) and OH^- (in base) [31,32]. Photocorrosion is a major problem for long-term PEC cells because of water splitting, which leads to the decomposition and fluctuation of photocurrent in a short time interval, especially in harsh conditions (strongly acidic or alkaline). However, a high ionic environment (low or high pH) is essential to minimize other challenges such as ohmic losses and localized pH gradient overpotentials in the PEC systems of separate photoelectrodes [33,34]. Therefore, ferroelectric materials with intrinsically stable properties even in harsh electrolyte are potential candidates for the generation of new PEC systems. Furthermore, the suitable alignment between the band edge potentials of the candidate materials and the relative decomposition potentials can promote stable PEC devices. Lastly, cost-effective materials along with earth-abundant elements are also required for a practical approach.

4.2. Ferroelectric-Based Materials in Photocathodes for Hydrogen

Promising photocathodes are generally p-type semiconductors and must meet some of the aforementioned requirements to generate the required cathodic current for water reduction. Single metallic oxides such as Cu_2O , CuO , and NiO are at the forefront of the p-type semiconductors that have been investigated as photocathodes for solar water splitting. However, these materials are hindered by some major shortcomings such as photocorrosion [35,36], low conduction band position [37–39] and wide bandgap (3.6–4.0 eV), along with the low potential of the valence band [40,41]. As a result, the PEC devices fabricated from conventional single semiconductors exhibit a limited photocurrent and low stability, thereby reducing their PEC performance. Therefore, the possibility of incorporating ferroelectrics into conventional oxide-based photocathodes is a novel and facile way to enhance their PEC activity. In this section, the review is focused on ferroelectric-based materials for photocathodes, which include ferroelectric ternary/quaternary metal oxides.

4.2.1. Ferroelectric Oxide Perovskites

Ternary Metal Oxides

(1) BiFeO_3

BiFeO_3 (BFO) is a well-known multiferroic material with a bandgap in the range of 2.2–2.7 eV, which has been researched extensively because it possesses a wide range of intriguing properties [42–51]. Many studies have been reported on the significant effect of polarization on band bending in BFO, which plays a crucial role in the photocatalytic activity for PEC water splitting. This enhanced charge separation is attributed to the intimate relation between band bending and the separation of photoexcited electron–hole pairs in the space charge region [52]. Depending on the fabrication method, BFO can exhibit properties of either an n or p-type semiconducting material, thereby playing a role as either an anodic or cathodic electrode in PEC water splitting [42,45,47,51].

Although BFO presents robust ferroelectricity and has attracted significant interest from researchers involved in PEC water-splitting research, there are two challenges that limit the tremendous potential of BFO as a photoelectrode material. The first issue is the low photocathodic current due to the rapid recombination of electron–hole pairs, which is required to achieve a better PEC performance. Another challenge is the rapid degradation during the PEC reaction [53,54]. Undoubtedly, the noble metal Pt is by far the best-performing photocathode for H_2 evolution to date [55]. Theoretically, a combination of BFO and a noble metal such as Pt is considered a good choice to facilitate H_2 generation reaction. This can be explained by the reduced charge recombination and enhanced electric field that is attributed to the Schottky barrier due to the different work functions between BFO and Pt as well as the localized surface plasmon resonance (LSPR) effect of these noble metals [56,57]. However, contact between Pt and BFO impedes the transfer of photoexcited electrons from an electrode surface to the electrolyte due to the Schottky upward barrier. Fortunately, the injection of a buffer layer between Pt and BFO has been discovered to overcome this shortcoming.

Gu et al. [53] inserted a porous carbon layer sandwiched between Pt and BFO to obtain a ITO/BFO/carbon/Pt photocathode in order to inhibit the formation of a BFO/Pt Schottky upward barrier. As a result, drastically enhanced photocathodic performance is achieved with a photocurrent density (J_o) and onset potential (V_{op}) up to $-235.4 \mu\text{A}/\text{cm}^2$ and 1.19 V versus reversible hydrogen electrode (RHE), respectively, while the values for a photocathode without a carbon interlayer are only $-61.6 \mu\text{A}/\text{cm}^2$ and 0.83 V versus RHE, respectively. More importantly, the BFO films were macroscopically poled to investigate the effect of the ferroelectric polarization on the PEC performance, and the results are reported in Figure 6. After poling, the J_o and V_{op} values increased significantly, which is attributed to the effective separation of the photogenerated carriers in the BFO films, thereby enhancing the PEC activity of the photocathodes.

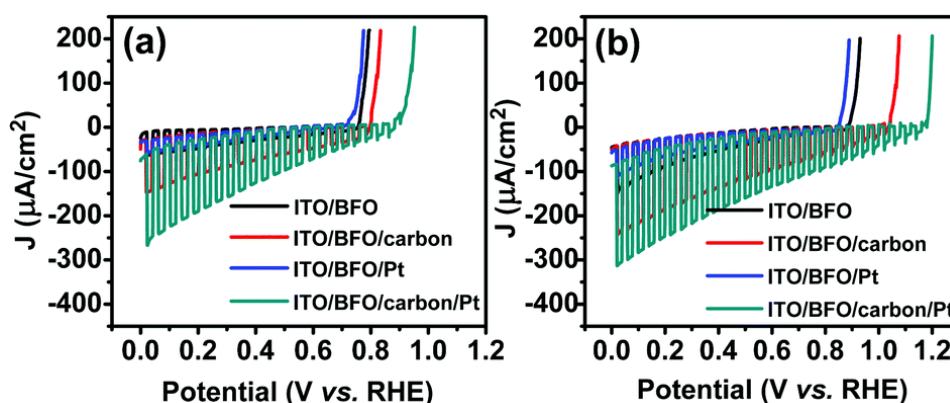


Figure 6. Photocurrent potential (J - V) curves of different BiFeO_3 (BFO)-based photocathodes before (a) and after (b) positively poling the BFO film [53]. Copyright 2017, Royal Society of Chemistry.

The novel configuration with carbon resulted in a reduced charge recombination and the facilitation of charge transfer by the removal of the upward barrier between Pt and BFO. Based on this result, an amorphous TiO_2 was chosen as a buffer layer to insert between BFO and Pt with the similar desire for the Schottky barrier [58]. As expected, the PEC yielded a J_0 of $-460 \mu\text{A}/\text{cm}^2$ at 0 V versus RHE and V_{op} of 1.25 V versus RHE under $100 \text{ mW}/\text{cm}^2$ Xe-lamp illumination. More importantly, the role of TiO_2 in stabilizing the photocathode is apparent with a 10-h continuous effective PEC reaction in an acid solution. Meanwhile, most of the BFO photocathodic performance is degradable within only 2 h of continuous reaction, even when measured using the neutral Na_2SO_4 electrolyte [53,54]. The limitation of the performance of PEC cells used BFO as photocathodes could be overcome by an interlayer TiO_2 as protection layer to avoid direct contact with its electrolyte. This interpretation could show a promising pathway to reduce cathodic photocorrosion at the semiconductor/electrolyte interface by employing a variety of protection layers on the photocathodes. To utilize a wide range of the visible light spectrum, tandem PEC systems composed of both photoanodes and photocathodes have been investigated in many recent studies [59,60]. Among many tandem architectures, the photocathodes based on the crystal Si-pn^+ were constructed with an improvement in PEC activity [61,62]. However, the efficiency is far from the desired value because of the remaining photoexcited electrons inside the holes of Si. In a recent report, Cheng et al. [54] overcame his shortcoming to fabricate a $\text{Si-pnn}^+/\text{ITO}/\text{Au}/\text{BFO}$ hybrid photocathode with enhanced photocurrent and onset potential by utilizing the local surface plasmon resonance (LSPR) effect of Au nanoparticles and the depolarization electric field of BFO.

(2) LaFeO_3

LaFeO_3 (LFO) is an n-type semiconducting perovskite oxide that has emerged as an attractive candidate for photoelectrochemical water splitting because of its many advantages, such as high stability under illumination in an aqueous environment, and abundant quantity of rare-earth element oxides [59,60]. The bandgap of LFO is estimated to be from 2.0 eV to 2.6 eV, which is small enough to utilize a portion of the visible spectrum light [39].

Although LFO has stood out as a promising perovskite oxide, it still has some drawbacks that limit its use as an effective photocathode for hydrogen production [63–67]. The LFO photocathode in PEC shows low photoresponse characteristics because of the lack of a sophisticated preparative technique [68]. The p-type LFO film, which is prepared by more sophisticated fabrication techniques such as pulsed laser deposition (PLD) and atomic layer deposition (ALD) as a photocathode coupling with an n-type Fe_2O_3 photoanode for stable water splitting, has assisted in the suppression of the aforementioned limitation [63,69]. High-quality LFO films and good back contacts resulted in the generation of a photocurrent density at 0 V versus RHE of $64.5 \mu\text{A}/\text{cm}^2$ under AM 1.5 G irradiation for

100 nm of LFO, while the reaction time was maintained for 120 h without any obvious decline of the rate of oxygen and hydrogen production [63]. In addition, under external bias, the Fe_2O_3 - LaFeO_3 system shows outstanding performance in both the development of the gas evolution rates and stability, even in alkaline conditions, in comparison with an Fe_2O_3 -Pt system. Furthermore, the modified LFO photocathode with high performance, especially its long-term stability and low cost, could be considered one of the promising candidates to replace the normal Pt photocathode in PEC systems.

Although the low photoresponse problem was solved by PLD instead of the sol-gel spin-coating method, the value of the photocurrent onset potential was ~ 1.0 V versus RHE, which is lower than the standard potential of 1.23 V for water electrolysis. Recent efforts to enhance the photoelectrochemical behavior of LFO has yielded many positive results. Díez-García et al. [70] synthesized metal-doped LFO thin film electrodes using the sol-gel method, resulting in a significant improvement in efficiency, with an onset potential as high as 1.4 V versus RHE. The enhancement of the efficiency in PCE devices is attributed to an increase of both majority carrier density and mobility by doping with a relatively large amount of Mg^{2+} and Zn^{2+} (5% with respect to the iron atoms).

In addition, it is reported that metal doping is an effective strategy for enhancing the p-type nature of the ternary oxides [71]. In particular, LFOs have been shown to exhibit both cathodic and anodic photocurrents depending on the specific conditions [72]. Although sophisticated fabrication techniques such as PLD can improve the PEC response of LFO photocathodes, the high cost and challenging technical requirements are still primary impediments. Recently, novel research in the preparation of nanostructured LFO thin films using an inexpensive spray-pyrolysis method resulted in outstanding results [73]. The fabricated photoelectrode yielded a photocurrent density of 0.16 mA/cm^2 at 0.26 V versus RHE, which is by far a more drastic enhancement compared to the PLD technique [63].

Interestingly, this is the first time that spontaneous hydrogen generation has been achieved using PEC water splitting without any external bias voltage using LFO as a single photoelectrode material. Admittedly, LFO is a potential candidate for a photocathode because of its stable characteristics in aqueous solutions, as well as its very positive onset potential values. However, further research should be performed to improve the slow kinetics of charge transfer, which favors recombination at surface trap states.

(3) SrTiO_3

Among the various ternary metal oxides, SrTiO_3 (STO), which is a stable n-type semiconductor with a bandgap value of 3.25 eV [74], has been utilized as a promising photoelectrode for splitting water into hydrogen and oxygen, with many outstanding properties. However, a wide bandgap limits light absorption to the UV region.

Since the first report by Wrighton et al. [75] on the usefulness of STO for light-assisted photocatalytic water splitting, numerous studies have focused on bandgap engineering [76–78] and the tuning of the charge separation ability [79–81] to overcome the aforementioned drawbacks and achieve effective photoelectrochemical water splitting. It is expected that a heterojunction of STO with a small bandgap material should be able to narrow the overall bandgap and help suppress the limitation of visible light absorption.

TiO_2 is a conventional n-type semiconductor, which is considered as the most promising photoanode material [82–85], and Cu_2O is one of the most investigated p-type semiconductors for PEC water-splitting. It is reported that loading Cu_2O particles on TiO_2 nanotube arrays can significantly improve visible light absorption compared with pure TiO_2 nanotubes [86]. Meanwhile, there is a similar valence and conduction band position between STO and TiO_2 , with a conduction band edge that is about 200 mV higher than TiO_2 [87]. Recently, Cu_2O has been combined with STO with controllable thickness to form a $\text{Cu}_2\text{O}/\text{STO}$ heterojunction photoelectrode, which has been proven to be effective in driving the separation of charge carriers by an electric field generated at the $\text{Cu}_2\text{O}/\text{STO}$ interface [88]. Under illumination, the $\text{Cu}_2\text{O}/\text{STO}$ photoelectrode presented a p-type photocurrent used for hydrogen generation. As expected, the $\text{Cu}_2\text{O}/\text{STO}$ heterojunction with an optimal thickness of 343 nm exhibited

a photocurrent density of 2.52 mA/cm^2 at 0.8 V versus saturated calomel electrode (SCE), which is 25 times higher than that of pristine Cu_2O (0.10 mA/cm^2 at 0.8 V versus SCE), as presented in Figure 7. This result is attributed to the synergy of broadening solar absorption and improved charge transportation in the $\text{Cu}_2\text{O}/\text{STO}$ heterojunction. In another report, the $\text{Cu}_2\text{O}/\text{STO}$ heterojunction photocathode was investigated using a less complicated method in which Cu_2O nanoparticles (NPs) were loaded onto the surface of STO nanocubes (NCs) through a facile deposition—precipitation technique [89].

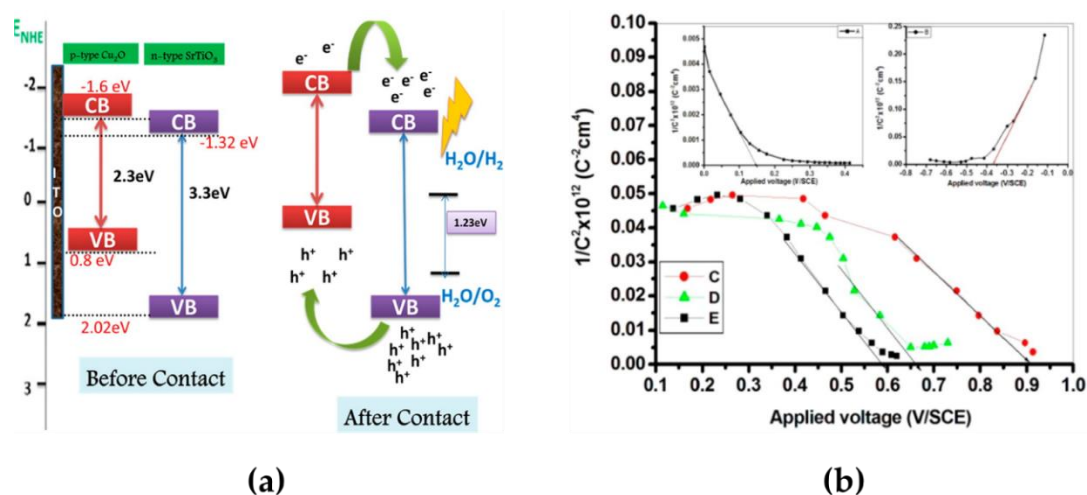


Figure 7. (a) Energy band diagram of Cu_2O and SrTiO_3 before and after formation of the p–n junction, (b) Photocurrent density vs. applied potential curve for (A) pristine Cu_2O and (C) 343 nm of $\text{Cu}_2\text{O}/\text{SrTiO}_3$ heterojunction [88]. Copyright 2014, American Chemical Society.

(4) PbTiO_3

PbTiO_3 (PTO) is a visible light active titania-based perovskite oxide that is well-known for its high ferroelectricity. It is a good candidate as a photocatalytic material in water splitting due to its bandgap value of 2.75 eV and suitable band structure, which assists in charge transfer and separation [90–92]. However, there are a limited number of studies on the application of PTO as a photoelectrode material with demonstrated higher photocatalytic activity for hydrogen evolution, especially in the case of PEC devices.

Recently, transition metal-doped PTO was investigated as a photocathode material for improving photogenerated electron transfer on the photocathode/electrolyte interface [92,93]. In particular, the $1 \text{ wt } \%$ Cu-doped PTO photoelectrode in an aqueous methanol solution under visible light irradiation ($\lambda \geq 400 \text{ nm}$) presented 2.5 times higher photocatalytic performance compared to PTO without Cu loading using the same configuration [92].

In another report, Hu et al. [93] modified the ITO/PTO photocathode using both Fe (III) doping and grafting, which resulted in a photocurrent increases of up to $220 \mu\text{A/cm}^2$ in comparison with $38 \mu\text{A/cm}^2$ of pure PTO photocathode. These enhancements were attributed to the change of band positions, which facilitated the transfer of photoinduced charge carriers. A similar phenomenon was observed for a fabricated Ag–Pt bimetallic catalyst on a ferroelectric PTO photocathode surface deposited on ITO quartz glass. As a result, the photocurrent density increased significantly from $60 \mu\text{A/cm}^2$ for pure PTO electrode to $202 \mu\text{A/cm}^2$ for the Ag–Pt electrode one under 0 V versus SCE, and with a 100 mW/cm^2 Xe lamp illumination [94].

Due to the superior performance of PTO in comparison with other TiO_2 -based perovskite-type oxide materials (BaTiO_3 , SrTiO_3) and their stability, some innovative synthesis methods have been introduced such as microwave-assisted synthesis [95,96] and nonhydrolytic sol-gel [97]. A promising

and effective PTO photocathode with higher photocurrent efficiency has been achieved using such facile and cost-effective synthesis methods.

(5) YFeO_3

YFeO_3 is one of the ferrite perovskites featuring a bandgap energy of approximately 2.3–2.4 eV. Although several studies have been performed on the utilization of YFeO_3 as a photocatalyst for water splitting [98–101], research on YFeO_3 as a photocathode material in PEC devices remains limited. YFeO_3 thin films are prepared by two different methodologies: nanoparticle thin film electrode via an ionic liquid protocol [68], and compact thin film electrode via a sol-gel method. Both types of electrodes have been evaluated for their PEC activity. They show exhibited cathodic photocurrent responses with an onset potential of 1.05 V versus RHE with complex dynamic features that should be addressed to application in PEC water splitting [102].

Quaternary Metal Oxides

Quaternary metal oxides, especially double perovskite materials featuring ferroelectric behavior, have been identified as promising candidates for solar energy to electricity conversion because of their efficient charge separation, which results from suitable control of the polarization-induced internal electric field [103,104]. $\text{Bi}_2\text{FeCrO}_6$ (BFCO) exhibiting multiferroic properties plays a role as a photocathode with a narrow bandgap (1.9–2.1 eV), and an appropriate conduction band position, which shows a twofold increase of the photocurrent density after negative poling, as presented in Figure 8 [105]. Recently, Shen et al. performed many studies on $\text{Pb}(\text{Zr,Ti})\text{O}_3$ (PZT) and revealed that ferroelectric PZT films deposited on indium tin oxide (ITO)-coated quartz glass [106,107] along with PZT films decorated with Ag nanoparticles on an ITO coated Si-pn⁺ junction [108] can function as stable and effective photocathodes for water splitting. More importantly, polarization switching can drive the photogenerated electrons transfer process, which then results in significantly enhanced PEC activity.

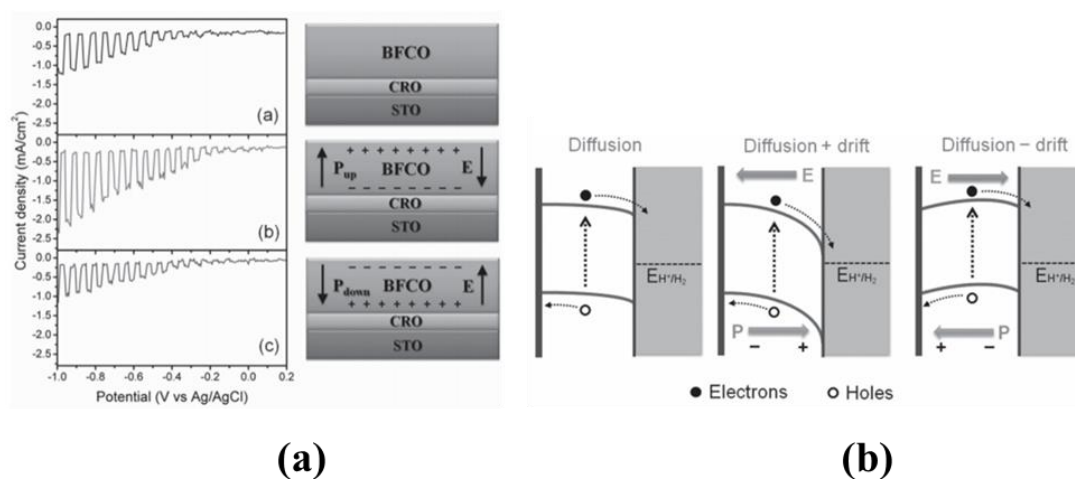


Figure 8. (a) Variations of the current density with applied voltage and (b) Simplified energy band diagrams of the PEC cell based on $\text{Bi}_2\text{FeCrO}_6$ (BFCO) thin film without polarization (left) and either negatively poled (middle) or positively poled (right) [105]. Copyright 2015, Wiley Online Library.

4.3. Ferroelectric-Based Materials in Photoanodes for Water

Photoanode materials, which possess bandgap values that utilize a wide range of visible light absorption, high carrier mobility, and the possibility of efficient charge transport and separation, generally stem from n-type semiconductors. In addition, they are cost-effective materials that have a long-term stability in aqueous solution, and are therefore considered promising candidates for

PEC water splitting. In this section, ferroelectric-based materials are incorporated in a photoanodic configuration with various nanostructures via optimal fabrication techniques.

4.3.1. Ferroelectric Oxide Perovskites

(1) BaTiO₃

BaTiO₃ (BTO) is an n-type semiconductor, and its ferroelectricity was discovered for the first time in 1945 by Wul and Goldman [109]. Subsequently, the relation between photocurrent efficiency and the change in the electrode potential for the photooxidation of water was first investigated by Kennedy [110] in 1976. This was a precursor to advanced studies on this promising ferroelectric material. Apart from possessing a favorable structure for water splitting [111], BTO is considered as a potential photoelectrode material because of its high stability in aqueous solution along with a suitable band edge position, and controllable electronic properties through lattice defect modification or oxygen stoichiometry [112,113]. However, the only disadvantage of BTO is a relatively large bandgap of 3.2 eV, which limits its absorption spectrum to the ultraviolet region [114].

Therefore, many previous reports [115,116] were focused on doping BTO with Fe to extend its photoresponse for effective PEC activity. More importantly, it was reported that the ferroelectric polarization in BTO could enhance PEC performance in comparison with pristine TiO₂. This is a result of the facilitation of the separation of photogenerated electron–hole pairs along with the effectiveness of tuning of the electronic band structure (i.e., upward band bending) in heterojunction-based PEC devices of TiO₂/BTO core/shell nanowire (NW) arrays as photoanodes [117]. However, the contribution of the ferroelectric polarization effect plays a predominant role, which is evidenced by numerous different measurements such as the PE hysteresis loop, dynamic contact electrostatic force microscopy (DC-EFM) characterization, and electric poling by different directions. As a result, the positive polarization switched by external electric field poling at the TiO₂/BTO (5 nm of thickness) interface yielded an optimal photocurrent density of water oxidation (1.30 mA/cm²) that was 67% higher than that of a photoanode without BTO (0.78 mA/cm²). This result hints at the tremendous potential of ferroelectric photoelectrodes in enhancing PEC performance.

(2) BiVO₄

Bismuth vanadate (BiVO₄) is an n-type semiconductor (bandgap value ~2.5 eV), which has been widely applied as a photoanode material in PEC cells because of its large absorbance range in the visible spectrum along with a suitable conduction band structure [118,119]. Based on its bandgap energy, BiVO₄ is able to generate a photocurrent density of ~7.5 mA/cm² and a theoretical solar-to-hydrogen conversion efficiency of 9.2% under AM 1.5 G conditions [120,121]. However, BiVO₄ suffers from poor surface catalytic reactivity and substantial recombination losses, which prevent it from achieving the theoretical maximum. With the aim of addressing these drawbacks, many strategies such as doping, morphology control, and the construction of heterojunction structures have been investigated in PEC devices containing BiVO₄ photoelectrodes.

Choi et al. [122] prepared nanoporous BiVO₄ photoanodes with dual-layer oxygen evolution catalysts (OEC), which is reported to alleviate bulk carrier recombination at the BiVO₄/OEC junction by creating a more favorable Helmholtz layer potential drop at the OEC/electrolyte junction. PEC devices containing BiVO₄/FeOOH/NiOOH photoanodes have been shown to yield a photocurrent density of 2.73 mA/cm² at a potential as low as 0.6 V versus RHE without any extrinsic doping and composition tuning. Subsequently, this author's group performed further mild annealing treatment of nanoporous BiVO₄ under N₂ flow that produced nitrogen doping and the generation of oxygen vacancies [123]. This is attributed to the enhanced major carrier density as well as the major carrier mobility of BiVO₄. The photocurrent was drastically improved to 4.16 ± 0.41 mA/cm², and the NiOOH/FeOOH/N-BiVO₄ photoanode manifested an applied biased photo-to-current efficiency (ABPE) of 2.0% under a bias of 0.6 V. In further investigations of the same BiVO₄/Fe(Ni)OOH tandem structure, further enhancement of

the photocurrent density up to 5.82 ± 0.36 mA/cm² at 1.23 V versus RHE was achieved by Mo-doping with a concentration of 3% on a nanocone FTO/BiVO₄ substrate [124].

In other studies [125–128], because WO₃ has well-known properties such as its low cost, high chemical stability, and good charge transport activity, BiVO₄ was coupled with this material to overcome the moderate charge transport feature of PEC cells fabricated from pure BiVO₄ to produce PEC cells with robust performance. Nevertheless, these studies at potentials as low as 0.6 V versus RHE still demonstrate charge separation efficiencies of less than 60%.

Kuang et al. [129] reported on a non-doped nanostructured BiVO₄ photoanode with a bimetallic NiFe-(oxy)hydroxide/borate(NiFeO_x-B₁) oxygen evolution catalyst as an efficient oxidation co-catalyst to achieve a solar energy conversion efficiency in excess of 2%. More importantly, a very high of incident photo-to-current efficiency (IPCE) of approximately 80% was achieved at a potential as low as 0.6 V versus RHE under front irradiation up to 460 nm, which is nearly twice of that of a previous nanoporous BiVO₄ electrode [122] without compromising other beneficial properties. Recently, Lee et al. [130] fabricated epitaxial BiVO₄ on a thin γ -WO₃ template layer deposited on a SrTiO₃ (001) substrate by pulsed laser deposition (PLD).

Although PLD was applied in the fabrication of a BiVO₄ photoanode electrode in PEC cells for the first time by Liu and Yan [131] in the last decade, it drew less attention at the time because of its very low photocurrent values, regardless of the high-quality films. However, the effect of the thin γ -WO₃ template layer on the effective charge transfer and increased active surface area of BiVO₄ accounted for the significantly enhanced photocurrent density (2.20 mA/cm²) at 1.23 V versus RHE, which is approximately 10 times higher than that of bare BiVO₄. This study highlighted that PLD combined with suitable BiVO₄ photoanode materials is a facile and versatile technique for producing good-quality electrodes for PEC water splitting.

(3) SrTiO₃

Titanium dioxide (TiO₂) was the first oxide used as a photoanode material for PEC water splitting and was discovered by Fujishima-Honda [13]. Until now, it has been one of the most attractive materials for PEC cells. However, TiO₂ absorbs only in the UV part of the spectrum because of its large bandgap [132], which exhibits low efficiency in water-splitting reactions when TiO₂ is used as a single photoanode [133–136].

SrTiO₃ (STO) is a perovskite oxide that shows considerable ferroelectricity [137,138] and possesses a favorable band edge structure that overlaps with the water redox potentials. In addition, the conduction band edge is more negative than TiO₂, as presented in Figure 9 [139]. Similar to TiO₂, STO responds only to the UV region and a negligible portion of the visible light. This has prevented it from being a good single photoanode candidate for PEC cells. As a result, STO has been doped with dopants, or coupled with TiO₂, which the aim of shifting the Fermi level of the dual-phase STO/TiO₂ composite [87], for application as a potential candidate for improving photoconversion efficiency.

Limited reports have focused on TO thin films with dopants such as (Cr, Rh, Ir, and Nb) [140–144]. However, a few of these studies have reported some drawbacks such as non-uniform doping and the insignificant effect of such dopants, or even the resulting instability because of the formation of IrO₂ [145]. Recently, further investigation into STO/TiO₂ photoanode materials has revealed some desirable outcomes [87,139,145–148]. Wysmulek et al. [136] studied a durable eutectic system made up of TiO₂ and STO as an active photoanode material for PEC cells. Under 600 mW/cm² of solar irradiation, the TiO₂/STO eutectic photoelectrode yielded a photocurrent density of up to 8.5 mA/cm² at 1.5 V versus NHE and stabilized after 30 h of testing. This result not only shows an improvement in the photocurrent density, it also showed a better long-term operation compared with Ir-doped STO (24 h) [145]. Thus, eutectic composite-based photoelectrodes are untapped components for PEC water splitting. In addition, the spontaneous electric polarization in STO can simultaneously enhance charge separation and hole transportation in TiO₂/STO core-shell nanowires (NWs) [146]. Compared to the TiO₂/BaTiO₃ ferroelectric PEC system [138], STO ferroelectric material shows better charge

mobility, which will facilitate hole migration inside the ferroelectric layer. Interestingly, the core shell with an optimal STO thickness of 10 nm generates the highest photocurrent density of 1.43 mA/cm² and has the charge-separation efficiency of 87.7% at 1.23 V versus RHE. This corresponds to an 83% and 79% improvement in comparison with pristine TiO₂ NWs. This study has paved the way for the application of semiconducting ferroelectric materials to further advance the development of ferroelectric PEC systems.

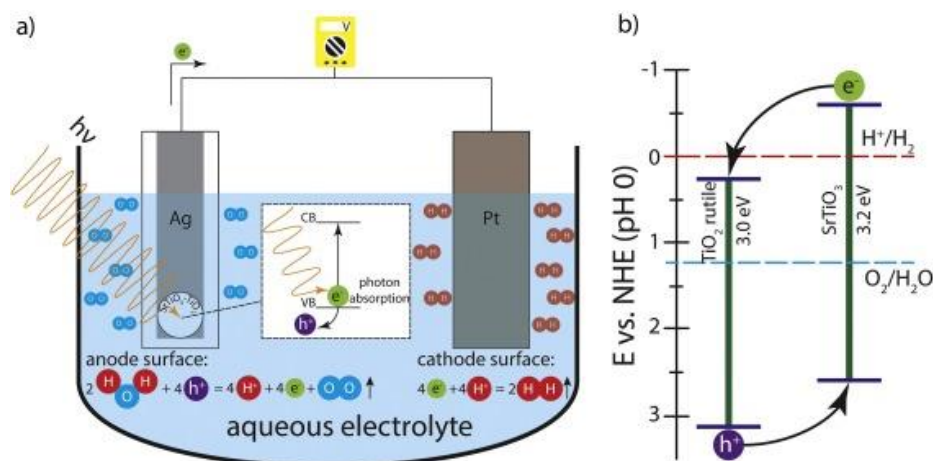


Figure 9. SrTiO₃-TiO₂ eutectic composite-based PEC cell. (a) A simplified PEC cell employing a eutectic system as the photoactive anode material. (b) Charge-carrier separation mechanism at the phase boundary, with bandgap positions and values with respect to electrochemical potential (E) vs. NHE based on [139,147,148]. Figure 9 [139] from Copyright 2017 Elsevier.

(4) BiFeO₃

The BiFeO₃ (BFO) ferroelectric material shows unique photovoltaic effects that result from large spontaneous polarization. This prominent characteristic develops a high built-in potential that effectively enhances the separation and drift of photogenerated carriers for application in PEC devices composed of BFO-containing photoelectrodes. In comparison with photocathodic materials, there are few reports regarding the application of BFO as photoanodic materials in PEC water splitting.

Very recently, Song et al. [4] reported on epitaxial BFO thin-film photoanodes with different crystallographic orientations including (111)_{pc}, (110)_{pc}, (001)_{pc}, and the consequence of the ferroelectric domain structures was also investigated. To investigate the difference among various crystallographic orientations on ferroelectric properties and the effect of different polarization states on photovoltaic performance, ferroelectric P-E hysteresis loop and polarization switching measurements were performed, respectively, as shown in Figure 10. The results revealed that in the absence of polarization, the charge energy band bending, which induces inefficient charge separation, was not observed. In contrast, an optimal PEC performance with (111)_{pc} BFO thin film under a downward polarization state was revealed. Previously, enhanced efficiency in a polycrystalline BFO photoanode also exhibited a similar mechanism when switching the polling bias from +8 V to -8 V [149]. This BFO thin film was based on the cost-effective technology of spin coating, instead of growing epitaxial BFO thin film using more sophisticated techniques including radio frequency (RF) and pulsed laser deposition (PLD) [150,151]. However, this limits their application in large-scale technology.

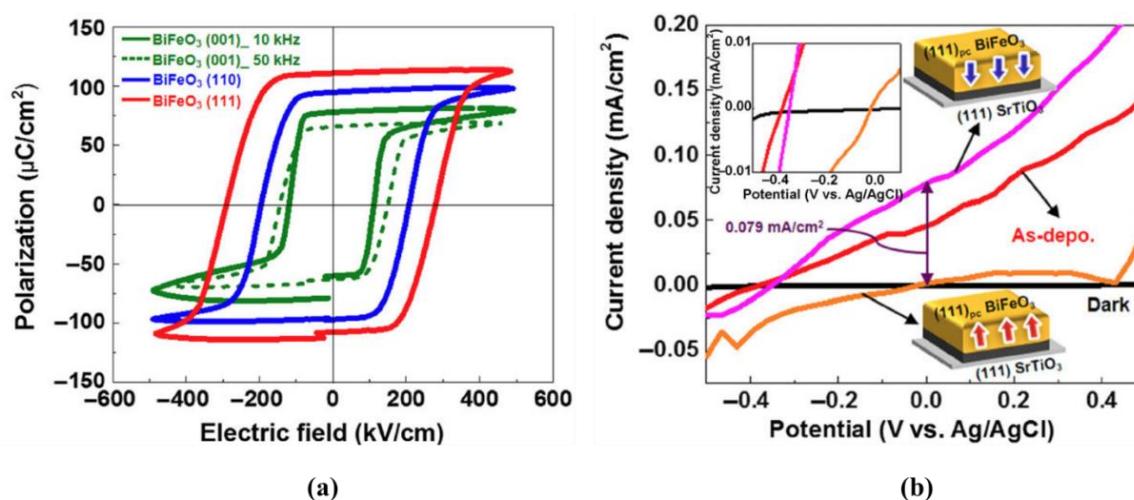


Figure 10. (a) P–E hysteresis loop for a 400-nm-thick epitaxial BiFeO₃ thin film with (001)_{pc} BFO at 10 kHz and 50 kHz frequencies and (110)_{pc}, (111)_{pc} BFO thin film at 10 kHz. (b) Polarization switching measurement of the 50-nm thick (111)_{pc} BFO thin film photoanodes in different polarization states. The inset shows the magnified portion for the onset potential [4]. Copyright 2018, Springer.

(5) PbTiO₃

Although a large number of studies have been performed based on PbTiO₃-containing materials as photocathodes in PEC cells for hydrogen production, photoanodes composed of PbTiO₃ (PTO) are increasingly of concern. Specifically, there are numerous reports on nanostructured PTO because of their superior PEC properties, which are related to their randomly shaped particles [152,153]. Moreover, many useful approaches based on heterojunctions from different semiconductors have resulted in improved photoactivity [127,154–158].

Based on these two interpretations, Jang et al. [159] synthesized vertically aligned core–shell PTO@TiO₂ heterojunction nanotube arrays fabricated on FTO glass by a three-step process that can help suppress the opaque photoanode problem reported in a previous study [91]. As expected, the directional charge transport in one-dimensional (1D) nanostructure and additional heterojunction effects between PTO and TiO₂ favor charge separation and enhanced PEC efficiency in PTO@TiO₂ photoanode-based systems. Recently, there was a report on the synthesis of nanotubular PTO-based photoanodes in PEC devices for the first time [160]. The investigation was performed with two synthetic electrodes of 1D nanotube arrays of PTO (NT–PTO) and Pt-dots@PTO nanotube arrays (PNT–PTO) in comparison with two reference electrodes made of PTO nanotubes (no Pt dots) and PTO powder (no nanotubes). The result presents that the NT–PTO photoanode achieved the highest photocurrent density of 64 μA/cm² at 1.05 V versus RHE. In comparison, the PTO powder-based photoelectrode exhibited a meager value of 8 μA/cm² at the same RHE potential. The enhanced PEC performance was elucidated by reducing the electron–hole recombination through the isolated oxidation sites at the external surface of the Pt-dots@PTO nanotubular structure.

4.3.2. Ferroelectric Chalcogenides

(1) CdS

Cadmium sulfide (CdS) is the most common ferroelectric chalcogenide investigated in PEC water splitting because of its narrow energy bandgap of 2.4 eV and suitable band edge position [157,158]. Despite these advantages, the CdS-based PEC devices showed a low performance because of inefficient charge transfer and separation [161–165].

Uniform carbon-coated CdS core–shell nanostructures are potentially useful as a facile and novel approach to overcome this challenge [166]. The enhanced performance is elucidated by the

substantially improved electron transfer, which results from the high electrical conductivity of the coated carbon layer on CdS. CdS widely couples with ZnO nanowires and nanorods as an ideal heterostructure in PEC devices that helps to suppress internal charge recombination and enhance solar-to-chemical conversion [167–169]. Accordingly, the development of ZnO/CdS nanotube arrays outperforms the previous structures with a larger specific surface, which results in a superior ability for charge extraction, especially in the case of nanoparticle plasmon metal addition [170,171].

Besides the common nanostructured CdS, a rare report on the versatile hierarchical structure of CdS film was investigated recently [172]. Zang et al. [173] grew screw-like SnO₂ nanosheets on rod-like single-crystalline SnO₂ nanowires deposited with CdS quantum dots in PEC cells that tend to move toward efficient PEC water splitting. This structure is a combination of both the fast charge transport path of 1D nanostructures and the high porosity and light absorption of 2D nanosheets, which will extend the perspective of high-performance PEC cells in the near future.

(2) ZnS

Zinc sulfide (ZnS) is regarded as one of the most important II–VI semiconductors, and is an appealing candidate for water splitting because of its own outstanding properties, which include an ability to generate mobile photoexcited charge carriers [174], fast electron transfer because of high CB potential, and high catalytic activity for H₂ generation under conditions without a co-catalyst [175,176]. However, the performance of pure ZnS-based photoelectrode in water-splitting devices is limited, because absorption is only in the UV region due to the wide bandgap value of 3.66 eV of this material [177]. Furthermore, overcoming the high charge recombination is also a serious challenge [178,179].

As a result, many modifications have been investigated for ZnS-based electrodes to increase visible light absorption. To enhance photocatalytic activity, transition metal-doped ZnS (Cu, Ni, Mo) or doping with GaN were investigated as potentially efficient photocatalysts to generate H₂ under visible light irradiation [180–182]. However, due to the remaining challenges of dopant introduction [181,183–186] an alternative method by controlling defects in nanostructured ZnS has been exploited through PLD to enhance the overall PEC properties of ZnS [187]. The fabrication of ZnS-based heterojunctions with other semiconductors for more advanced designs has been considered to enhance PEC performance for water splitting.

Typically, the ZnO/ZnS heterostructure has drawn tremendous attention because of the extended visible absorption that it affords and its appropriate alignment [188–192]. Among ZnO/ZnS heterostructures with different morphologies such as nanowires [193] and nanorings [194] synthesized by means of chemical processes, the PEC behavior is scarcely introduced by anodization, which facilitates electron–hole separation, and consequently, the enhancement of photoelectrochemical activity for water splitting [195]. Moreover, the design of sandwich-structured ZnO/ZnS photoanodes with a third component, such as noble metals Au or graphite-like carbon nitride (C₃N₄), have been demonstrated with significantly superior PEC activity compared to those of a pristine ZnO photoanode [196,197]. Nevertheless, the remaining challenge is the wide bandgap of the ZnO/ZnS heterojunction, which still limits large-range visible light absorption. The systems that result from coupling ZnS with narrow bandgap chalcogenide CdS exhibit much higher performance than those of every single material-based system [198–202].

4.3.3. Hybrid Halide Ferroelectric CH₃NH₃PbI₃ Perovskite Tandem System Approach

Tandem cell configuration is a facile and novel approach to address the limitation of single or heterojunction PEC devices for water splitting. Organic–inorganic hybrid perovskite CH₃NH₃PbI₃ has attracted tremendous attention in perovskite solar cells (PSCs) because of their superb light-harvesting characteristics, large electron/hole diffusion lengths, and high crystallinity [203–207]. Based on the latest research, the certified highest efficiency of PSCs is 22.1% fabricated on limited to very small areas (~1 cm²) [208]. Ferroelectric domains have been observed in CH₃NH₃PbI₃, despite the centrosymmetric

structure of this perovskite material, which is ascribed to the reduced symmetry of molecular CH_3NH_3^+ dipoles [209,210].

Recently, Luo et al. [211] demonstrated two perovskite solar cells connected in series as a tandem cell that can serve as a separated and external power supply for water splitting, as presented in Figure 11. Although this device can achieve a high photocurrent density of $\sim 10 \text{ mA/cm}^2$, the electrodes were not directly settled in the photoreactions. Moreover, the rapid fluctuation of the photocurrent due to the instability of the perovskite was a challenge that could be addressed by encapsulation techniques to achieve intriguing PEC tandem systems. More recently, Da et al. reported on a $\text{CH}_3\text{NH}_3\text{PbI}_3$ -based photoanode coated by an ultrathin Ni layer for the first time with a much enhanced photocurrent density of 12 mA/cm^2 , which is attributed to the improved photoabsorption of $\text{CH}_3\text{NH}_3\text{PbI}_3$ [212]. In their report, a Ni top layer played a decisive role in the enhancement of the photocurrent density and assisted in the suppression of the instability of perovskite PEC tandem systems in water; this evokes many promising perspectives in the development of hybrid perovskite-based tandem cells.

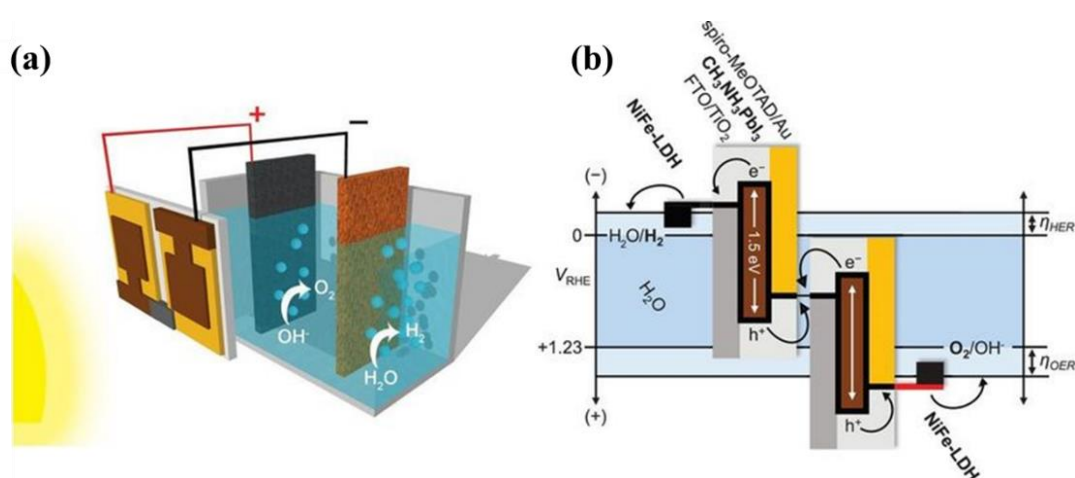


Figure 11. Combination of the perovskite tandem cell with NiFe DLH/Ni foam electrodes for water splitting, (a) Schematic diagram of the water-splitting device, (b) A generalized energy schematic of the perovskite tandem cell for water splitting [211]. Copyright from 2014, American Association for the Advancement of Science.

5. Conclusions and Outlook

Interest in solar water splitting is on the rise, which is in line with a general trend of increasing environmental awareness. Based on state-of-the-art reports, amazing progress in solar water splitting has been demonstrated, including the upgrade of systems, and the development of new electrode materials and their structure. To perform high-efficiency solar water splitting, the materials used in the different systems have to satisfy three conditions. They should have: an appropriate bandgap energy, a suitable position of the bandgap, and chemical stability. The ideal material has a bandgap of approximately $\sim 2.0\text{--}2.2 \text{ eV}$, which can absorb about 40% of the total incident sunlight. The conduction band (CB) and valence band (VB) of the materials should be higher—between the water reduction level and below the oxidation level of water—in order to induce the water decomposition reaction. At present, no materials have been identified that meet all of the requirements for water decomposition reactions.

In this review, we introduced various ferroelectric materials for solar water splitting with high STH efficiency. Ferroelectric materials have been known to be very stable and strong for chemical and physical applications, and their bandgap could be narrowed by doping and/or substitution. Even though solar water splitting systems with ferroelectric materials are the newest technology and have attracted important new research into hydrogen generation, until now, there has not

yet been much research performed on ferroelectric materials for use in water-splitting systems. Solar water-splitting systems with ferroelectrics are expected as significant advances in the process of hydrogen generation, with high STH efficiencies compared to other materials.

Author Contributions: C.W.B. had the main idea for the article. S.K., N.T.N. performed the literature search and the writing of the manuscript in consultation with C.W.B. All authors discussed the concept of review and commented on the manuscript.

Funding: This research was supported by the Korea Electric Power Corporation. (Grant number: R17XA05-10) and Creative Materials Discovery Program through the National Research Foundation of Korea (NRF) funded by the Ministry of Science and ICT (2017M3D1A1040828), and by the grants from the National Research Foundation of Korea (NRF) funded by the Ministry of Science, ICT, and Future Planning (NRF-2016R1C1B1014649)

Conflicts of Interest: The authors declare no conflict of interest.

References

1. Lopes, T.; Dias, P.; Andrade, L.; Mendes, A. An innovative photoelectrochemical lab device for solar water splitting. *Sol. Energy Mater. Sol. Cells* **2014**, *128*, 399–410. [[CrossRef](#)]
2. Ngoh, S.K.; Njomo, D. An overview of hydrogen gas production from solar energy. *Renew. Sustain. Energy Rev.* **2012**, *16*, 6782–6792. [[CrossRef](#)]
3. Sun, J.W.; Zhong, D.K.; Gamelin, D.R. Composite photoanodes for photoelectrochemical solar water splitting. *Energy Environ. Sci.* **2010**, *3*, 1252–1261. [[CrossRef](#)]
4. Song, J.; Kim, T.L.; Lee, J.; Cho, S.Y.; Cha, J.; Jeong, S.Y.; An, H.; Kim, W.S.; Jung, Y.S.; Park, J.; et al. Domain-engineered BiFeO₃ thin-film photoanodes for highly enhanced ferroelectric solar water splitting. *Nano Res.* **2018**, *11*, 642–655. [[CrossRef](#)]
5. Pan, H.; Zhu, S.; Lou, X.; Mao, L.; Lin, J.; Tian, F.; Zhang, D. Graphene-based photocatalysts for oxygen evolution from water. *RSC Adv.* **2015**, *5*, 6543–6552. [[CrossRef](#)]
6. Zhao, J.; Wang, X.; Xu, Z.C.; Loo, J.S.C. Hybrid catalysts for photoelectrochemical reduction of carbon dioxide: A prospective review on semiconductor/metal complex co-catalyst systems. *J. Mater. Chem. A* **2014**, *2*, 15228–15233. [[CrossRef](#)]
7. Jang, J.S.; Kim, H.G.; Lee, J.S. Heterojunction semiconductors: A strategy to develop efficient photocatalytic materials for visible light water splitting. *Catal. Today* **2012**, *185*, 270–277. [[CrossRef](#)]
8. Vilanova, A.; Lopes, T.; Spenke, C.; Wullenkord, M.; Mendes, A. Optimized photoelectrochemical tandem cell for solar water splitting. *Energy Storage Mater.* **2018**, *13*, 175–188. [[CrossRef](#)]
9. Tentu, R.D.; Basu, S. Photocatalytic water splitting for hydrogen production. *Curr. Opin. Electrochem.* **2017**, *5*, 56–62. [[CrossRef](#)]
10. Li, R. Latest progress in hydrogen production from solar water splitting via photocatalysis, photoelectrochemical, and photovoltaic-photoelectrochemical solutions. *Chin. J. Catal.* **2017**, *38*, 5–12. [[CrossRef](#)]
11. Ismail, A.A.; Bahnemann, D.W. Photochemical splitting of water for hydrogen production by photocatalysis: A review. *Sol. Energy Mater. Sol. Cells* **2014**, *128*, 85–101. [[CrossRef](#)]
12. Jiang, C.R.; Moniz, S.J.A.; Wang, A.G.; Zhang, T.; Tang, J.W. Photoelectrochemical devices for solar water splitting-materials and challenges. *Chem. Soc. Rev.* **2017**, *46*, 4645–4660. [[CrossRef](#)] [[PubMed](#)]
13. Honda, A.; Honda, K. Electrochemical photolysis of water at a semiconductor electrode. *Nat. Commun.* **1972**, *238*, 37–38.
14. Alfaifi, B.Y.; Ullah, H.; Alfaifi, S.; Tahir, A.A.; Mallick, T.K. Photoelectrochemical Solar Water Splitting: From Basic Principles to Advanced Devices. *Veruscr. Funct. Nanomater.* **2018**, *2*, 1–26. [[CrossRef](#)]
15. Chen, Z.; Dinh, D.; Miller, E. Chapter 3 Experimental Considerations. In *Photoelectrochemical Water Splitting*, 1st ed.; Springer: New York, NY, USA, 2013; pp. 17–44, ISBN 978-1-4614-8298-7.
16. Paillard, C.; Bai, X.F.; Infante, I.C.; Guennou, M.; Geneste, G.; Alexe, M.; Kreisel, J.; Dkhil, B. Photovoltaics with ferroelectrics: Current status and beyond. *Adv. Mater.* **2016**, *28*, 5153–5168. [[CrossRef](#)] [[PubMed](#)]
17. Wick, R.; Tilley, S.D. Photovoltaic and photoelectrochemical solar energy conversion with Cu₂O. *J. Phys. Chem. C* **2015**, *119*, 26243–26257. [[CrossRef](#)]
18. Tablero, C. Photovoltaic application of the multiferroic Bi₂FeCrO₆ double perovskite. *Sol. Energy* **2016**, *137*, 173–178. [[CrossRef](#)]

19. Archer, M.D. Photovoltaics and photoelectrochemistry: Similarities and differences. *Physica E* **2002**, *14*, 61–64. [[CrossRef](#)]
20. Lopez-Varo, P.; Bertoluzzi, L.; Bisquert, J.; Alexe, M.; Coll, M.; Huang, J.S.; Juan, A.J.T.; Kirchartz, T.; Nechache, R.; Rosei, F.; et al. Physical aspects of ferroelectric semiconductors for photovoltaic solar energy conversion. *Phys. Rep.* **2016**, *653*, 1–40. [[CrossRef](#)]
21. Spanier, J.E.; Fridkin, V.M.; Rappe, A.M.; Akbashev, A.R.; Polemi, A.; Qi, Y.B.; Gu, Z.Q.; Young, S.M.; Hawley, C.J.; Imbrenda, D.; et al. Power conversion efficiency exceeding the shockley-queisser limit in a ferroelectric insulator. *Nat. Photonics* **2016**, *10*, 611–616. [[CrossRef](#)]
22. Bonke, S.A.; Wiechen, M.; MacFarlane, D.R.; Spiccia, L. Renewable fuels from concentrated solar power: Towards practical artificial photosynthesis. *Energy Environ. Sci.* **2015**, *8*, 2791–2796. [[CrossRef](#)]
23. Jia, J.Y.; Seitz, L.C.; Benck, J.D.; Huo, Y.J.; Chen, Y.S.; Ng, J.W.D.; Bilir, T.; Harris, J.S.; Jaramillo, T.F. Solar water splitting by photovoltaic-electrolysis with a solar-to-hydrogen efficiency over 30%. *Nat. Commun.* **2016**, *7*, 1–6. [[CrossRef](#)] [[PubMed](#)]
24. Chu, S.; Li, W.; Yan, Y.; Hamann, T.; Shin, I.; Wang, D.; Mi, Z. Roadmap on solar water splitting: Current status and future prospects. *Nano Futures* **2017**, *1*, 1–29. [[CrossRef](#)]
25. Jacobsson, T.J.; Fjallstrom, V.; Edoff, M.; Edvinsson, T. Sustainable solar hydrogen production: From photoelectrochemical cells to pv-electrolyzers and back again. *Energy Environ. Sci.* **2014**, *7*, 2056–2070. [[CrossRef](#)]
26. Tamirat, A.G.; Rick, J.; Dubale, A.A.; Su, W.N.; Hwang, B.J. Using hematite for photoelectrochemical water splitting: A review of current progress and challenges. *Nanoscale Horiz.* **2016**, *1*, 243–267. [[CrossRef](#)]
27. Butler, K.T.; Frost, J.M.; Walsh, A. Ferroelectric materials for solar energy conversion: Photoferroics revisited. *Energy Environ. Sci.* **2015**, *8*, 838–848. [[CrossRef](#)]
28. Khan, M.A.; Nadeem, M.A.; Idrissn, H. Ferroelectric polarization effect on surface chemistry and photo-catalytic activity: A review. *Surf. Sci. Rep.* **2016**, *71*, 1–31. [[CrossRef](#)]
29. Li, L.; Salvador, P.A.; Rohrer, G.S. Photocatalysts with internal electric fields. *Nanoscale* **2014**, *6*, 24–42. [[CrossRef](#)] [[PubMed](#)]
30. Sivula, K.; Krol, R.V.D. Semiconducting materials for photoelectrochemical energy conversion. *Nat. Rev. Mater.* **2016**, *1*, 1–17. [[CrossRef](#)]
31. Walter, M.G.; Warren, E.L.; Mckone, J.R.; Boettcher, S.W.; Mi, Q.; Santori, E.A.; Lewis, N.S. Solar Water Splitting Cells. *Chem. Rev.* **2010**, *110*, 6446–6473. [[CrossRef](#)] [[PubMed](#)]
32. Burke, M.S.; Enman, L.J.; Batchellor, A.S.; Zou, S.; Boettcher, S.W. Oxygen Evolution Reaction Electrocatalysis on Transition Metal Oxides and (Oxy)hydroxides: Activity Trends and Design Principles. *Chem. Mater.* **2015**, *27*, 7549–7558. [[CrossRef](#)]
33. Jin, J.; Walczak, K.; Singh, M.R.; Karp, C.; Lewis, N.S.; Xiang, C. An experimental and modeling/simulation-based evaluation of the efficiency and operational performance characteristics of an integrated, membrane-free, neutral pH solar-driven water-splitting system. *Energy Environ. Sci.* **2014**, *7*, 3371–3380. [[CrossRef](#)]
34. Seger, B.; Castelli, I.E.; Vesborg, P.C.K.; Jacobsen, K.W.; Hansen, O.; Chorkendorff, I. 2-Photon tandem device for water splitting: Comparing photocathode first *versus* photoanode first designs. *Energy Environ. Sci.* **2014**, *7*, 2397–2413. [[CrossRef](#)]
35. Hara, M.; Kondo, T.; Komoda, M.; Ikeda, S.; Shinohara, K.; Tanaka, A.; Kondo, J.N.; Domen, K. Cu₂O as a photocatalyst for overall water splitting under visible light irradiation. *Chem. Commun.* **1998**, 357–358. [[CrossRef](#)]
36. Jongh, P.E.D.; Vanmaekelbergh, D.; Kelly, J.J. Cu₂O: A catalyst for the photochemical decomposition of water? *Chem. Commun.* **1999**, 1069–1070. [[CrossRef](#)]
37. Chauhan, D.; Satsangi, V.R.; Dass, S.; Shrivastav, R. Preparation and characterization of nanostructured CuO thin films for photoelectrochemical splitting of water. *Bull. Mater. Sci.* **2006**, *29*, 709–716.
38. Koffyberg, F.P.; Benko, F.A. A photoelectrochemical determination of the position of the conduction and valence band edges of p-type CuO. *J. Appl. Phys.* **1982**, *53*, 1173–1177. [[CrossRef](#)]
39. Hsu, Y.K.; Yu, C.H.; Lin, H.H.; Chen, Y.C.; Lin, Y.G. Template synthesis of copper oxide nanowires for photoelectrochemical hydrogen generation. *J. Electroanal. Chem.* **2013**, *704*, 19–23. [[CrossRef](#)]
40. Gupta, R.K.; Ghosh, K.; Kahol, P.K. Fabrication and characterization of NiO/ZnO p-n junctions by pulsed laser deposition. *Physica E* **2009**, *41*, 617–620. [[CrossRef](#)]

41. Dong, Y.M.; Chen, Y.M.; Jiang, P.P.; Wang, G.L.; Wu, X.M.; Wu, R.X.; Zhang, C. Efficient and stable MoS₂/CdSe/NiO photocathode for photoelectrochemical hydrogen generation from water. *Chem. Asian J.* **2015**, *10*, 1660–1667. [[CrossRef](#)] [[PubMed](#)]
42. Yilmaz, P.; Yeo, D.; Chang, H.; Loh, L.; Dunn, S. Perovskite BiFeO₃ thin film photocathode performance with visible light activity. *Nanotechnology* **2016**, *27*, 1–9. [[CrossRef](#)] [[PubMed](#)]
43. Yi, H.T.; Choi, T.; Choi, S.G.; Oh, Y.S.; Cheong, S.W. Mechanism of the switchable photovoltaic effect in ferroelectric BiFeO₃. *Adv. Mater.* **2011**, *23*, 3403–3407. [[CrossRef](#)] [[PubMed](#)]
44. Ren, Y.; Nan, F.; You, L.; Zhou, Y.; Wang, Y.Y.; Wang, J.L.; Su, X.D.; Shen, M.R.; Fang, L. Enhanced photoelectrochemical performance in reduced graphene oxide/BiFeO₃ heterostructures. *Small* **2017**, *13*, 1–7. [[CrossRef](#)] [[PubMed](#)]
45. Quynh, L.T.; Van, C.N.; Bitla, Y.; Chen, J.W.; Do, T.H.; Tzeng, W.Y.; Liao, S.C.; Tsai, K.A.; Chen, Y.C.; Wu, C.L.; et al. Self-assembled BiFeO₃- ϵ -Fe₂O₃ vertical heteroepitaxy for visible light photoelectrochemistry. *Adv. Energy Mater.* **2016**, *6*. [[CrossRef](#)]
46. Liu, Q.; Zhou, Y.; You, L.; Wang, J.L.; Shen, M.R.; Fang, L. Enhanced ferroelectric photoelectrochemical properties of polycrystalline BiFeO₃ film by decorating with ag nanoparticles. *Appl. Phys. Lett.* **2016**, *108*, 1–5. [[CrossRef](#)]
47. Ji, W.; Yao, K.; Lim, Y.F.; Liang, Y.C.; Suwardi, A. Epitaxial ferroelectric BiFeO₃ thin films for unassisted photocatalytic water splitting. *Appl. Phys. Lett.* **2013**, *103*, 1–4. [[CrossRef](#)]
48. Hauser, A.J.; Zhang, J.; Mier, L.; Ricciardo, R.A.; Woodward, P.M.; Gustafson, T.L.; Brillson, L.J.; Yang, F.Y. Characterization of electronic structure and defect states of thin epitaxial BiFeO₃ films by UV-visible absorption and cathodoluminescence spectroscopies. *Appl. Phys. Lett.* **2008**, *92*, 1–3. [[CrossRef](#)]
49. Gupta, S.; Medwal, R.; Limbu, T.B.; Katiyar, R.K.; Pavunny, S.P.; Tomar, M.; Morell, G.; Gupta, V.; Katiyar, R.S. Graphene/semiconductor silicon modified BiFeO₃/indium tin oxide ferroelectric photovoltaic device for transparent self-powered windows. *Appl. Phys. Lett.* **2015**, *107*. [[CrossRef](#)]
50. Cho, S.; Jang, J.W.; Zhang, W.R.; Suwardi, A.; Wang, H.Y.; Wang, D.W.; MacManus-Driscoll, J.L. Single-crystalline thin films for studying intrinsic properties of BiFeO₃-SrTiO₃ solid solution photoelectrodes in solar energy conversion. *Chem. Mater.* **2015**, *27*, 6635–6641. [[CrossRef](#)]
51. Chen, X.Y.; Yu, T.; Gao, F.; Zhang, H.T.; Liu, L.F.; Wang, Y.M.; Li, Z.S.; Zou, Z.G.; Liu, J.M. Application of weak ferromagnetic BiFeO₃ films as the photoelectrode material under visible-light irradiation. *Appl. Phys. Lett.* **2007**, *91*. [[CrossRef](#)]
52. Mohan, S.; Subramanian, B.; Bhaumik, I.; Gupta, P.K.; Jaisankar, S.N. Nanostructured Bi_{1-x}Gd_xFeO₃—A multiferroic photocatalyst on its sunlight driven photocatalytic activity. *RSC Adv.* **2014**, *4*, 16871–16878. [[CrossRef](#)]
53. Gu, S.L.; Zhou, X.X.; Zheng, F.G.; Fang, L.; Dong, W.; Shen, M.R. Improved photocathodic performance in Pt catalyzed ferroelectric BiFeO₃ films sandwiched by a porous carbon layer. *Chem. Commun.* **2017**, *53*, 7052–7055. [[CrossRef](#)] [[PubMed](#)]
54. Cheng, X.R.; Shen, H.Y.; Dong, W.; Zheng, F.G.; Fang, L.A.; Su, X.D.; Shen, M.R. Nano-au and ferroelectric polarization mediated Si/ITO/BiFeO₃ tandem photocathode for efficient H₂ production. *Adv. Mater. Interfaces* **2016**, *3*, 1–7. [[CrossRef](#)]
55. Kang, D.H.; Kim, T.W.; Kubota, S.R.; Cardiel, A.C.; Cha, H.G.; Choi, K.S. Electrochemical synthesis of photoelectrodes and catalysts for use in solar water splitting. *Chem. Rev.* **2015**, *115*, 12839–12887. [[CrossRef](#)] [[PubMed](#)]
56. Atwater, H.A.; Polman, A. Plasmonics for improved photovoltaic devices. *Nat. Mater.* **2010**, *9*, 205–213. [[CrossRef](#)] [[PubMed](#)]
57. Takai, A.; Kamat, P.V. Capture, store, and discharge. Capture, store, and discharge. Shuttling photogenerated electrons across TiO₂-silver interface. *ACS Nano* **2011**, *5*, 7369–7376. [[CrossRef](#)] [[PubMed](#)]
58. Shen, H.Y.; Zhou, X.X.; Dong, W.; Su, X.D.; Fang, L.A.; Wu, X.; Shen, M.R. Dual role of TiO₂ buffer layer in Pt catalyzed BiFeO₃ photocathodes: Efficiency enhancement and surface protection. *Appl. Phys. Lett.* **2017**, *111*. [[CrossRef](#)]
59. Prévot, M.S.; Sivula, K. Photoelectrochemical tandem cells for solar water splitting. *J. Phys. Chem. C* **2013**, *117*, 17879–17893. [[CrossRef](#)]

60. Hu, S.; Xiang, C.X.; Haussener, S.; Berger, A.D.; Lewis, N.S. An analysis of the optimal band gaps of light absorbers in integrated tandem photoelectrochemical water-splitting systems. *Energy Environ. Sci.* **2013**, *6*, 2984–2993. [[CrossRef](#)]
61. Fan, R.L.; Dong, W.; Fang, L.A.; Zheng, F.G.; Su, X.D.; Zou, S.; Huang, J.; Wang, X.S.; Shen, M.R. Stable and efficient multi-crystalline n(+)p silicon photocathode for H₂ production with pyramid-like surface nanostructure and thin Al₂O₃ protective layer. *Appl. Phys. Lett.* **2015**, *106*. [[CrossRef](#)]
62. Fan, R.L.; Min, J.W.; Li, Y.; Su, X.D.; Zou, S.; Wang, X.S.; Shen, M.R. N-type silicon photocathodes with Al-doped rear p(+) emitter and Al₂O₃-coated front surface for efficient and stable H₂ production. *Appl. Phys. Lett.* **2015**, *106*. [[CrossRef](#)]
63. Yu, Q.; Meng, X.G.; Wang, T.; Li, P.; Liu, L.Q.; Chang, K.; Liu, G.G.; Ye, J.H. A highly durable p-LaFeO₃/n-Fe₂O₃ photocell for effective water splitting under visible light. *Chem. Commun.* **2015**, *51*, 3630–3633. [[CrossRef](#)] [[PubMed](#)]
64. Wheeler, G.P.; Choi, K.S. Photoelectrochemical properties and stability of nanoporous p-type LaFeO₃ photoelectrodes prepared by electrodeposition. *ACS Energy Lett.* **2017**, *2*, 2378–2382. [[CrossRef](#)]
65. Ding, J.L.; Lu, X.M.; Shu, H.M.; Xie, J.M.; Zhang, H. Microwave-assisted synthesis of perovskite ReFeO₃ (Re: La, Sm, Eu, Gd) photocatalyst. *Mater. Sci. Eng. B* **2010**, *171*, 31–34. [[CrossRef](#)]
66. Parida, K.M.; Reddy, K.H.; Martha, S.; Das, D.P.; Biswal, N. Fabrication of nanocrystalline LaFeO₃: An efficient sol-gel auto-combustion assisted visible light responsive photocatalyst for water decomposition. *Int. J. Hydrogen Energy* **2010**, *35*, 12161–12168. [[CrossRef](#)]
67. Tijare, S.N.; Joshi, M.V.; Padole, P.S.; Mangrulkar, P.A.; Rayalu, S.S.; Labhsetwar, N.K. Photocatalytic hydrogen generation through water splitting on nano-crystalline LaFeO₃ perovskite. *Int. J. Hydrogen Energy* **2012**, *37*, 10451–10456. [[CrossRef](#)]
68. Celorrio, V.; Bradley, K.; Weber, O.J.; Hall, S.R.; Fermin, D.J. Photoelectrochemical properties of LaFeO₃ nanoparticles. *ChemElectroChem* **2014**, *1*, 1667–1671. [[CrossRef](#)]
69. Peng, Q.; Wang, J.; Feng, Z.J.; Du, C.; Wen, Y.W.; Shan, B.; Chen, R. Enhanced photoelectrochemical water oxidation by fabrication of p-LaFeO₃/n-Fe₂O₃ heterojunction on hematite nanorods. *J. Phys. Chem. C* **2017**, *121*, 12991–12998. [[CrossRef](#)]
70. Diez-Garcia, M.I.; Gómez, R. Metal doping to enhance the photoelectrochemical behavior of LaFeO₃ photocathodes. *ChemSusChem* **2017**, *10*, 2457–2463. [[CrossRef](#)] [[PubMed](#)]
71. Perkins, J.D.; Paudel, T.R.; Zakutayev, A.; Ndione, P.F.; Parilla, P.A.; Young, D.L.; Lany, S.; Ginley, D.S.; Zunger, A.; Perry, N.H.; et al. Inverse design approach to hole doping in ternary oxides: Enhancing p-type conductivity in cobalt oxide spinels. *Phys. Rev. B* **2011**, *84*, 1–8. [[CrossRef](#)]
72. Peng, Q.; Wang, J.; Wen, Y.W.; Shan, B.; Chen, R. Surface modification of LaFeO₃ by co-pi electrochemical deposition as an efficient photoanode under visible light. *RCS Adv.* **2016**, *6*, 26192–26198. [[CrossRef](#)]
73. Pawar, G.S.; Tahir, A.A. Unbiased spontaneous solar fuel production using stable LaFeO₃ photoelectrode. *Sci. Rep.* **2018**, *8*, 1–9. [[CrossRef](#)] [[PubMed](#)]
74. Cardona, M. Optical Properties and Band Structure of SrTiO₃ and BaTiO₃. *Phys. Rev.* **1965**, *140*, A651–A655. [[CrossRef](#)]
75. Wrighton, M.S.; Ellis, A.B.; Wolczanski, P.T.; Morse, D.L.; Abrahamson, H.B.; Ginley, D.S. Strontium titanate photoelectrodes. Efficient photoassisted electrolysis of water at zero applied potential. *J. Am. Chem. Soc.* **1976**, *98*, 2774–2779. [[CrossRef](#)]
76. Yu, H.G.; Irie, H.; Hashimoto, K. Conduction band energy level control of titanium dioxide: Toward an efficient visible-light-sensitive photocatalyst. *J. Am. Chem. Soc.* **2010**, *132*, 6898–6899. [[CrossRef](#)] [[PubMed](#)]
77. Ouyang, S.X.; Ye, J.H. β-AgAl_{1-x}Ga_xO₂ solid-solution photocatalysts: Continuous modulation of electronic structure toward high-performance visible-light photoactivity. *J. Am. Chem. Soc.* **2011**, *133*, 7757–7763. [[CrossRef](#)] [[PubMed](#)]
78. Wang, D.F.; Pierre, A.; Kibria, M.G.; Cui, K.; Han, X.G.; Bevan, K.H.; Guo, H.; Paradis, S.; Hakima, A.R.; Mi, Z.T. Wafer-level photocatalytic water splitting on GaN nanowire arrays grown by molecular beam epitaxy. *Nano Lett.* **2011**, *11*, 2353–2357. [[CrossRef](#)] [[PubMed](#)]
79. Nolan, M. Surface modification of TiO₂ with metal oxide nanoclusters: A route to composite photocatalytic materials. *Chem. Commun.* **2011**, *47*, 8617–8619. [[CrossRef](#)] [[PubMed](#)]

80. Tada, H.; Jin, Q.; Nishijima, H.; Yamamoto, H.; Fujishima, M.; Okuoka, S.; Hattori, T.; Sumida, Y.; Kobayashi, H. Titanium(iv) dioxide surface-modified with iron oxide as a visible light photocatalyst. *Angew. Chem. Int. Ed.* **2011**, *50*, 3501–3505. [[CrossRef](#)] [[PubMed](#)]
81. Yu, H.; Irie, H.; Shimodaira, Y.; Hosogi, Y.; Kuroda, Y.; Miyauchi, M.; Hashimoto, K. An efficient visible-light-sensitive Fe(III)-grafted TiO₂ photocatalyst. *J. Phys. Chem. C* **2010**, *114*, 16481–16487. [[CrossRef](#)]
82. Ni, M.; Leung, M.K.H.; Leung, D.Y.C.; Sumathy, K. A review and recent developments in photocatalytic water-splitting using TiO₂ for hydrogen production. *Renew. Sustain. Energy Rev.* **2007**, *11*, 401–425. [[CrossRef](#)]
83. Roy, P.; Berger, S.; Schmuki, P. TiO₂ nanotubes: Synthesis and applications. *Angew. Chem. Int. Ed.* **2011**, *50*, 2904–2939. [[CrossRef](#)] [[PubMed](#)]
84. Lee, K.; Mazare, A.; Schmuki, P. One-dimensional titanium dioxide nanomaterials: Nanotubes. *Chem. Rev.* **2014**, *114*, 9385–9454. [[CrossRef](#)] [[PubMed](#)]
85. Tian, J.; Zhao, Z.H.; Kumar, A.; Boughton, R.I.; Liu, H. Recent progress in design, synthesis, and applications of one-dimensional TiO₂ nanostructured surface heterostructures: A review. *Chem. Soc. Rev.* **2014**, *43*, 6920–6937. [[CrossRef](#)] [[PubMed](#)]
86. Zhang, J.Y.; Zhu, H.L.; Zheng, S.K.; Pan, F.; Wang, T.M. TiO₂ film/Cu₂O microgrid heterojunction with photocatalytic activity under solar light irradiation. *ACS Appl. Mater. Interfaces* **2009**, *1*, 2111–2114. [[CrossRef](#)] [[PubMed](#)]
87. Zhang, J.; Bang, J.H.; Tang, C.C.; Kamat, P.V. Tailored TiO₂-SrTiO₃ heterostructure nanotube arrays for improved photoelectrochemical performance. *ACS Nano* **2010**, *4*, 387–395. [[CrossRef](#)] [[PubMed](#)]
88. Sharma, D.; Upadhyay, S.; Satsangi, V.R.; Shrivastav, R.; Waghmare, U.V.; Dass, S. Improved photoelectrochemical water splitting performance of Cu₂O/SrTiO₃ heterojunction photoelectrode. *J. Phys. Chem. C* **2014**, *118*, 25320–25329. [[CrossRef](#)]
89. Liu, C.B.; Li, P.; Wu, G.L.; Luo, B.F.; Lin, S.; Ren, A.; Shi, W.D. Enhanced photoelectrochemical and photocatalytic activity by Cu₂O/SrTiO₃ p-n heterojunction via a facile deposition-precipitation technique. *RSC Adv.* **2015**, *5*, 33938–33945. [[CrossRef](#)]
90. Arney, D.; Watkins, T.; Maggard, P.A. Effects of particle surface areas and microstructures on photocatalytic H₂ and O₂ production over PbTiO₃. *J. Am. Ceram. Soc.* **2011**, *94*, 1483–1489. [[CrossRef](#)]
91. Yang, Y.; Wang, X.H.; Zhong, C.F.; Sun, C.K.; Yao, G.F.; Li, L.T. Synthesis and growth mechanism of lead titanate nanotube arrays by hydrothermal method. *J. Am. Ceram. Soc.* **2008**, *91*, 3388–3390. [[CrossRef](#)]
92. Reddy, K.H.; Parida, K. Fabrication, characterization, and photoelectrochemical properties of Cu-doped PbTiO₃ and its hydrogen production activity. *ChemCatChem* **2013**, *5*, 3812–3820. [[CrossRef](#)]
93. Hu, Y.X.; Dong, W.; Zheng, F.G.; Fang, L.; Shen, M.R. Fe(III) doped and grafted PbTiO₃ film photocathode with enhanced photoactivity for hydrogen production. *Appl. Phys. Lett.* **2014**, *105*, 1–4. [[CrossRef](#)]
94. Wang, Y.; Dong, W.; Zheng, F.; Fang, L.; Shen, M. Improved Photocathodic Properties of Ferroelectric PbTiO₃ Films Using Ag-Pt Bimetallic Catalyst. *Energy Environ. Focus* **2015**, *4*, 95–100. [[CrossRef](#)]
95. Tabari, T.; Singh, D.; Calisan, A.; Ebadi, M.; Tavakkoli, H.; Caglar, B. Microwave assisted synthesis of La_{1-x}Ca_xMnO₃ (x = 0, 0.2 and 0.4): Structural and capacitance properties. *Ceram. Int.* **2017**, *43*, 15970–15977. [[CrossRef](#)]
96. Jamali, S.S.; Singh, D.; Tavakkoli, H.; Kaveh, F.; Tabari, T. Microwave-assisted synthesis of nanostructured perovskite-type oxide with efficient photocatalytic activity against organic reactants in gaseous and aqueous phases. *Mater. Sci. Semicond. Process* **2017**, *64*, 47–54. [[CrossRef](#)]
97. Tabari, T.; Ebadi, M.; Singh, D.; Caglar, B.; Yagci, M.B. Efficient synthesis of perovskite-type oxide photocathode by nonhydrolytic sol-gel method with an enhanced photoelectrochemical activity. *J. Alloys Compd.* **2018**, *750*, 248–257. [[CrossRef](#)]
98. Tang, P.S.; Chen, H.F.; Cao, F.; Pan, G.X. Magnetically recoverable and visible-light-driven nanocrystalline YFeO₃ photocatalysts. *Catal. Sci. Technol.* **2011**, *1*, 1145–1148. [[CrossRef](#)]
99. Zhang, Y.W.; Yang, J.X.; Xu, J.F.; Gao, Q.Y.; Hong, Z.L. Controllable synthesis of hexagonal and orthorhombic YFeO₃ and their visible-light photocatalytic activities. *Mater. Lett.* **2012**, *81*, 1–4. [[CrossRef](#)]
100. Chen, Y.Y.; Yang, J.; Wang, X.L.; Feng, F.Y.; Zhang, Y.M.; Tang, Y. Synthesis YFeO₃ by salt-assisted solution combustion method and its photocatalytic activity. *J. Ceram. Soc. Jpn.* **2014**, *122*, 146–150. [[CrossRef](#)]
101. Lu, X.M.; Xie, J.M.; Shu, H.M.; Liu, J.; Yin, C.Q.; Lin, J.M. Microwave-assisted synthesis of nanocrystalline YFeO₃ and study of its photoactivity. *Mater. Sci. Eng. B* **2007**, *138*, 289–292. [[CrossRef](#)]

102. Díez-García, M.I.; Celorrio, V.; Calvillo, L.; Tiwari, D.; Gomez, R.; Fermin, D.J. YFeO₃ photocathodes for hydrogen evolution. *Electrochim. Acta* **2017**, *246*, 365–371. [[CrossRef](#)]
103. Glass, A.M.; von der Linde, D.; Auston, D.H.; Negran, T.J. Excited state polarization, bulk photovoltaic effect and the photorefractive effect in electrically polarized media. *J. Electron. Mater.* **1975**, *4*, 915–943. [[CrossRef](#)]
104. Fridkin, V.M. Bulk photovoltaic effect in noncentrosymmetric crystals. *Crystallogr. Rep.* **2001**, *46*, 654–658. [[CrossRef](#)]
105. Li, S.; AlOtaibi, B.; Huang, W.; Mi, Z.T.; Serpone, N.; Nechache, R.; Rosei, F. Epitaxial Bi₂FeCrO₆ multiferroic thin film as a new visible light absorbing photocathode material. *Small* **2015**, *11*, 4018–4026. [[CrossRef](#)] [[PubMed](#)]
106. Zhang, M.; Jiang, C.X.; Dong, W.; Zheng, F.G.; Fang, L.; Su, X.D.; Shen, M.R. Composition dependence of the photochemical reduction of Ag⁺ by as-grown Pb(Zr_xTi_{1-x})O₃ films on indium tin oxide electrode. *Appl. Phys. Lett.* **2013**, *103*, 1–4. [[CrossRef](#)]
107. Wang, C.Y.; Cao, D.W.; Zheng, F.G.; Dong, W.; Fang, L.; Su, X.D.; Shen, M.R. Photocathodic behavior of ferroelectric Pb(Zr,Ti)O₃ films decorated with silver nanoparticles. *Chem. Commun.* **2013**, *49*, 3769–3771. [[CrossRef](#)] [[PubMed](#)]
108. Cheng, X.R.; Dong, W.; Zheng, F.G.; Fang, L.; Shen, M.R. Enhanced photocathodic behaviors of Pb(Zr_{0.20}Ti_{0.80})O₃ films on Si substrates for hydrogen production. *Appl. Phys. Lett.* **2015**, *106*, 1–4. [[CrossRef](#)]
109. Wul, B.; Goldman, J.M. Ferroelectric switching in BaTiO₃ ceramics. *CR Acad. Sci. URSS* **1946**, *51*, 21.
110. Kennedy, J.H.; Frese, K.W. Photo-oxidation of water at Barium Titanate electrodes. *J. Electrochem. Soc.* **1976**, *123*, 1683–1686. [[CrossRef](#)]
111. Zielinska, B.; Borowiak-Palen, E.; Kalenczuk, R.J. Photocatalytic hydrogen generation over alkaline-earth titanates in the presence of electron donors. *Int. J. Hydrogen Energy* **2008**, *33*, 1797–1802. [[CrossRef](#)]
112. Dholam, R.; Patel, N.; Adami, M.; Miotello, A. Hydrogen production by photocatalytic water-splitting using Cr- or Fe-doped TiO₂ composite thin films photocatalyst. *Int. J. Hydrogen Energy* **2009**, *39*, 5337–5346. [[CrossRef](#)]
113. Toupin, J.; Strub, H.; Kressmann, S.; Boudot, M.; Artero, V.; Laberty-Robert, C. Engineering n-p junction for photoelectrochemical hydrogen production. *Phys. Chem. Chem. Phys.* **2017**, *19*, 30675–30682. [[CrossRef](#)] [[PubMed](#)]
114. Maruska, H.P.; Ghosh, A.K. Transition-metal dopants for extending the response of titanate photoelectrolysis anodes. *Sol. Energy Mater. Sol. Cells* **1979**, *1*, 237–247. [[CrossRef](#)]
115. Upadhyay, R.K.; Sharma, D. Fe doped BaTiO₃ sensitized by Fe₃O₄ nanoparticles for improved photoelectrochemical response. *Mater. Res. Express* **2018**, *5*, 1–9. [[CrossRef](#)]
116. Upadhyay, S.; Shrivastava, J.; Solanki, A.; Choudhary, S.; Sharma, V.; Kumar, P.; Singh, N.; Satsangi, V.R.; Shrivastav, R.; Waghmare, U.V.; et al. Enhanced photoelectrochemical response of BaTiO₃ with Fe doping: Experiments and first-principles analysis. *J. Phys. Chem. C* **2011**, *115*, 24373–24380. [[CrossRef](#)]
117. Yang, W.G.; Yu, Y.H.; Starr, M.B.; Yin, X.; Li, Z.D.; Kvit, A.; Wang, S.F.; Zhao, P.; Wang, X.D. Ferroelectric polarization-enhanced photoelectrochemical water splitting in TiO₂-BaTiO₃ core-shell nanowire photoanodes. *Nano Lett.* **2015**, *15*, 7574–7580. [[CrossRef](#)] [[PubMed](#)]
118. Kudo, A.; Omori, K.; Kato, H. A novel aqueous process for preparation of crystal form-controlled and highly crystalline BiVO₄ powder from layered vanadates at room temperature and its photocatalytic and photophysical properties. *J. Am. Chem. Soc.* **1999**, *121*, 11459–11467. [[CrossRef](#)]
119. Park, Y.; McDonald, K.J.; Choi, K.S. Progress in bismuth vanadate photoanodes for use in solar water oxidation. *Chem. Soc. Rev.* **2013**, *42*, 2321–2337. [[CrossRef](#)] [[PubMed](#)]
120. Abdi, F.F.; van de Krol, R. Nature and light dependence of bulk recombination in co-pi-catalyzed BiVO₄ photoanodes. *J. Phys. Chem. C* **2012**, *116*, 9398–9404. [[CrossRef](#)]
121. Tokunaga, S.; Kato, H.; Kudo, A. Selective preparation of monoclinic and tetragonal BiVO₄ with scheelite structure and their photocatalytic properties. *Chem. Mater.* **2001**, *13*, 4624–4628. [[CrossRef](#)]
122. Kim, T.W.; Choi, K.S. Nanoporous BiVO₄ Photoanodes with Dual-Layer Oxygen Evolution Catalysts for Solar Water Splitting. *Science* **2014**, *343*, 990–994. [[CrossRef](#)] [[PubMed](#)]
123. Kim, T.W.; Ping, Y.; Galli, G.A.; Choi, K.S. Simultaneous enhancements in photon absorption and charge transport of bismuth vanadate photoanodes for solar water splitting. *Nat. Commun.* **2015**, *6*, 1–10. [[CrossRef](#)] [[PubMed](#)]

124. Qiu, Y.C.; Liu, W.; Chen, W.; Chen, W.; Zhou, G.M.; Hsu, P.C.; Zhang, R.F.; Liang, Z.; Fan, S.S.; Zhang, Y.G.; et al. Efficient solar-driven water splitting by nanocone BiVO₄-perovskite tandem cells. *Sci. Adv.* **2016**, *2*, 1–8. [[CrossRef](#)] [[PubMed](#)]
125. Rao, P.M.; Cai, L.L.; Liu, C.; Cho, I.S.; Lee, C.H.; Weisse, J.M.; Yang, P.D.; Zheng, X.L. Simultaneously efficient light absorption and charge separation in WO₃/BiVO₄ core/shell nanowire photoanode for photoelectrochemical water oxidation. *Nano Lett.* **2014**, *14*, 1099–1105. [[CrossRef](#)] [[PubMed](#)]
126. Pihosh, Y.; Turkevych, I.; Mawatari, K.; Asai, T.; Hisatomi, T.; Uemura, J.; Tosa, M.; Shimamura, K.; Kubota, J.; Domen, K.; et al. Nanostructured WO₃/BiVO₄ photoanodes for efficient photoelectrochemical water splitting. *Small* **2014**, *10*, 3692–3699. [[CrossRef](#)] [[PubMed](#)]
127. Hong, S.J.; Lee, S.; Jang, J.S.; Lee, J.S. Heterojunction BiVO₄/WO₃ electrodes for enhanced photoactivity of water oxidation. *Energy Environ. Sci.* **2011**, *4*, 1781–1787. [[CrossRef](#)]
128. Van, C.N.; Do, T.H.; Chen, J.W.; Tzeng, W.Y.; Tsai, K.A.; Song, H.L.; Liu, H.J.; Lin, Y.C.; Chen, Y.C.; Wu, C.L.; et al. WO₃ mesocrystal-assisted photoelectrochemical activity of BiVO₄. *NPG Asia Mater.* **2017**, *9*. [[CrossRef](#)]
129. Kuang, Y.B.; Jia, Q.X.; Nishiyama, H.; Yamada, T.; Kudo, A.; Domen, K. A front-illuminated nanostructured transparent BiVO₄ photoanode for > 2% efficient water splitting. *Adv. Energy Mater.* **2016**, *6*. [[CrossRef](#)]
130. Song, J.; Cha, J.; Lee, M.G.; Jeong, H.W.; Seo, S.; Yoo, J.A.; Kim, T.L.; Lee, J.; No, H.; Kim, D.H.; et al. Template-engineered epitaxial BiVO₄ photoanodes for efficient solar water splitting. *J. Mater. Chem. A* **2017**, *5*, 18831–18838. [[CrossRef](#)]
131. Liu, Z.K.; Yan, F. The application of bismuth-based oxides in organic-inorganic hybrid photovoltaic devices. *J. Am. Ceram. Soc.* **2012**, *95*, 1944–1948. [[CrossRef](#)]
132. Chen, X.; Mao, S.S. Titanium dioxide nanomaterials: Synthesis, properties, modifications, and applications. *Chem. Rev.* **2007**, *107*, 2891–2959. [[CrossRef](#)] [[PubMed](#)]
133. Mohapatra, S.K.; Misra, M. Enhanced photoelectrochemical generation of hydrogen from water by 2,6-dihydroxyantraquinone-functionalized titanium dioxide nanotubes. *J. Phys. Chem. C* **2007**, *111*, 11506–11510. [[CrossRef](#)]
134. Mohapatra, S.K.; Misra, M.; Mahajan, V.K.; Raja, K.S. Design of a Highly Efficient Photoelectrolytic Cell for Hydrogen Generation by Water Splitting: Application of TiO_{2-x}C_x Nanotubes as a Photoanode and Pt/TiO₂ Nanotubes as a Cathode. *J. Phys. Chem. C* **2007**, *111*, 8677–8685. [[CrossRef](#)]
135. Ruan, C.M.; Paulose, M.; Varghese, O.K.; Grimes, C.A. Enhanced photo electrochemical-response in highly ordered TiO₂ nanotube-arrays anodized in boric acid containing electrolyte. *Sol. Energy Mater. Sol. Cells* **2006**, *90*, 1283–1295. [[CrossRef](#)]
136. Mor, G.K.; Shankar, K.; Paulose, M.; Varghese, O.K.; Grimes, C.A. Enhanced Photocleavage of Water Using Titania Nanotube Arrays. *Nano Lett.* **2005**, *5*, 191–195. [[CrossRef](#)] [[PubMed](#)]
137. Haeni, J.H.; Irvin, P.; Chang, W.; Uecker, R.; Reiche, P.; Li, Y.L.; Choudhury, S.; Tian, W.; Hawley, M.E.; Craigo, B.; et al. Room-temperature ferroelectricity in strained SrTiO₃. *Nature* **2004**, *430*, 758–761. [[CrossRef](#)] [[PubMed](#)]
138. Lee, J.H.; Selloni, A. TiO₂/Ferroelectric Heterostructures as Dynamic Polarization-Promoted Catalysts for Photochemical and Electrochemical Oxidation of Water. *Phys. Rev. Lett.* **2014**, *112*, 196102. [[CrossRef](#)] [[PubMed](#)]
139. Wismulek, K.; Sar, J.; Osewski, P.; Orłinski, K.; Kolodziejak, K.; Trenczek-Zajac, A.; Radecka, M.; Pawlak, D.A. A SrTiO₃-TiO₂ eutectic composite as a stable photoanode material for photoelectrochemical hydrogen production. *Appl. Catal. B* **2017**, *206*, 538–546. [[CrossRef](#)]
140. Kawasaki, S.; Nakatsuji, K.; Yoshinobu, J.; Komori, F.; Takahashi, R.; Lippmaa, M.; Mase, K.; Kudo, A. Epitaxial Rh-doped SrTiO₃ thin film photocathode for water splitting under visible light irradiation. *Appl. Phys. Lett.* **2012**, *101*, 1–4. [[CrossRef](#)]
141. Jiao, Z.B.; Chen, T.; Xiong, J.Y.; Wang, T.; Lu, G.X.; Ye, J.H.; Bi, Y.P. Visible-light-driven photoelectrochemical and photocatalytic performances of Cr-doped SrTiO₃/TiO₂ heterostructured nanotube arrays. *Sci. Rep.* **2013**, *3*, 1–6. [[CrossRef](#)] [[PubMed](#)]
142. Modak, B.; Ghosh, S.K. Enhancement of Visible Light Photocatalytic Activity of SrTiO₃: A Hybrid Density Functional Study. *J. Phys. Chem. C* **2015**, *119*, 23503–23514. [[CrossRef](#)]
143. Sangle, A.L.; Singh, S.; Jian, J.; Bajpe, S.R.; Wang, H.Y.; Khare, N.; MacManus-Driscoll, J.L. Very high surface area mesoporous thin films of SrTiO₃ grown by pulsed laser deposition and application to efficient photoelectrochemical water splitting. *Nano Lett.* **2016**, *16*, 7338–7345. [[CrossRef](#)] [[PubMed](#)]

144. Cen, J.J.; Wu, Q.Y.; Yan, D.H.; Tao, J.; Kisslinger, K.; Liu, M.Z.; Orlov, A. Photoelectrochemical water splitting with a SrTiO₃:Nb/SrTiO₃ n⁺-n homojunction structure. *Phys. Chem. Chem. Phys.* **2017**, *19*, 2760–2767. [[CrossRef](#)] [[PubMed](#)]
145. Kawasaki, S.; Takahashi, R.; Yamamoto, T.; Kobayashi, M.; Kumigashira, H.; Yoshinobu, J.; Komori, F.; Kudo, A.; Lippmaa, M. Photoelectrochemical water splitting enhanced by self-assembled metal nanopillars embedded in an oxide semiconductor photoelectrode. *Nat. Commun.* **2016**, *7*, 1–6. [[CrossRef](#)] [[PubMed](#)]
146. Wu, F.; Yu, Y.H.; Yang, H.; German, L.N.; Li, Z.Q.; Chen, J.G.; Yang, W.G.; Huang, L.; Shi, W.M.; Wang, L.J.; et al. Simultaneous Enhancement of Charge Separation and Hole Transportation in a TiO₂-SrTiO₃ Core-Shell Nanowire Photoelectrochemical System. *Adv. Mater.* **2017**, *29*, 1–7. [[CrossRef](#)] [[PubMed](#)]
147. Scanlon, D.O.; Dunnill, C.W.; Buckeridge, J.; Shevlin, S.A.; Logsdail, A.J.; Woodley, S.M.; Catlow, C.R.A.; Powell, M.J.; Palgrave, R.G.; Parkin, I.P.; et al. Band alignment of rutile and anatase TiO₂. *Nat. Mater.* **2013**, *12*, 798–801. [[CrossRef](#)] [[PubMed](#)]
148. Marschall, R. Semiconductor Composites: Strategies for Enhancing Charge Carrier Separation to Improve Photocatalytic Activity. *Adv. Funct. Mater.* **2014**, *24*, 2421–2440. [[CrossRef](#)]
149. Cao, D.W.; Wang, Z.J.; Nasori Wen, L.Y.; Mi, Y.; Lei, Y. Switchable Charge-Transfer in the Photoelectrochemical Energy-Conversion Process of Ferroelectric BiFeO₃ Photoelectrodes. *Angew. Chem. Int. Ed.* **2014**, *126*, 11027–11031. [[CrossRef](#)] [[PubMed](#)]
150. Ji, W.; Yao, K.; Liang, Y.C. Bulk Photovoltaic Effect at Visible Wavelength in Epitaxial Ferroelectric BiFeO₃ Thin Films. *Adv. Mater.* **2010**, *22*, 1763–1766. [[CrossRef](#)] [[PubMed](#)]
151. Bhatnagar, A.; Chaudhuri, A.R.; Kim, Y.H.; Hesse, D.; Alexe, M. Role of domain walls in the abnormal photovoltaic effect in BiFeO₃. *Nat. Commun.* **2013**, *4*, 1–8. [[CrossRef](#)]
152. Jun, H.; Im, B.; Kim, J.Y.; Im, Y.O.; Jang, J.W.; Kim, E.S.; Kim, J.Y.; Kang, H.J.; Hong, S.J.; Lee, J.S. Photoelectrochemical water splitting over ordered honeycomb hematite electrodes stabilized by alumina shielding. *Energy Environ. Sci.* **2012**, *5*, 6375–6382. [[CrossRef](#)]
153. Kim, J.Y.; Magesh, G.; Youn, D.H.; Jang, J.W.; Kubota, J.; Domen, K.; Lee, J.S. Single-crystalline, wormlike hematite photoanodes for efficient solar water splitting. *Sci. Rep.* **2013**, *3*, 1–8. [[CrossRef](#)] [[PubMed](#)]
154. Zhong, M.; Ma, Y.H.; Oleynikov, P.; Domen, K.; Delaunay, J.J. A conductive ZnO-ZnGaON nanowire-array-on-a-film photoanode for stable and efficient sunlight water splitting. *Energy Environ. Sci.* **2014**, *7*, 1693–1699. [[CrossRef](#)]
155. Hou, Y.; Zuo, F.; Dagg, A.; Feng, P.Y. A Three-Dimensional Branched Cobalt-Doped α -Fe₂O₃ Nanorod/MgFe₂O₄ Heterojunction Array as a Flexible Photoanode for Efficient Photoelectrochemical Water Oxidation. *Angew. Chem. Int. Ed.* **2013**, *52*, 1248–1252. [[CrossRef](#)] [[PubMed](#)]
156. Kumar, S.G.; Rao, K.S.R.K. Physics and chemistry of CdTe/CdS thin film heterojunction photovoltaic devices: Fundamental and critical aspects. *Energy Environ. Sci.* **2014**, *7*, 45–102. [[CrossRef](#)]
157. Wang, M.Y.; Sun, L.; Lin, Z.Q.; Cai, J.H.; Xie, K.P.; Lin, C.J. p-n Heterojunction photoelectrodes composed of Cu₂O-loaded TiO₂ nanotube arrays with enhanced photoelectrochemical and photoelectrocatalytic activities. *Energy Environ. Sci.* **2013**, *6*, 1211–1220. [[CrossRef](#)]
158. Jang, J.S.; Hwang, D.W.; Lee, J.S. CdS-AgGaS₂ photocatalytic diodes for hydrogen production from aqueous Na₂S/Na₂SO₃ electrolyte solution under visible light ($\lambda \geq 420$ nm). *Catal. Today* **2007**, *120*, 174–181. [[CrossRef](#)]
159. Jang, J.S.; Ahn, C.W.; Won, S.S.; Kim, J.H.; Choi, W.; Lee, B.S.; Yoon, J.H.; Kim, H.G.; Lee, J.S. Vertically Aligned Core-Shell PbTiO₃@TiO₂ Heterojunction Nanotube Array for Photoelectrochemical and Photocatalytic Applications. *J. Phys. Chem. C* **2017**, *121*, 15063–15070. [[CrossRef](#)]
160. Ahn, C.W.; Borse, P.H.; Kim, J.H.; Kim, J.Y.; Jang, J.S.; Cho, C.R.; Yoon, J.H.; Lee, B.S.; Bae, J.S.; Kim, H.G.; et al. Effective charge separation in site-isolated Pt-nanodot deposited PbTiO₃ nanotube arrays for enhanced photoelectrochemical water splitting. *Appl. Catal. B* **2018**, *224*, 804–809. [[CrossRef](#)]
161. Li, C.M.; Ahmed, T.; Ma, M.G.; Edvinsson, T.; Zhu, J.F. A facile approach to ZnO/Cds nanoarrays and their photocatalytic and photoelectrochemical properties. *Appl. Catal. B* **2013**, *138*, 175–183. [[CrossRef](#)]
162. Liu, Z.; Wang, Y.; Wang, B.; Li, Y.B.; Liu, Z.C.; Han, J.H.; Guo, K.Y.; Li, Y.J.; Cui, T.; Han, L.; et al. PEC electrode of ZnO nanorods sensitized by CdS with different size and its photoelectric properties. *Int. J. Hydrogen Energy* **2013**, *38*, 10226–10234. [[CrossRef](#)]

163. Xu, Y.; Zhao, W.W.; Xu, R.; Shi, Y.M.; Zhang, B. Synthesis of ultrathin CdS nanosheets as efficient visible-light-driven water splitting photocatalysts for hydrogen evolution. *Chem. Commun.* **2013**, *49*, 9803–9805. [[CrossRef](#)] [[PubMed](#)]
164. Pareek, A.; Purbia, R.; Paik, P.; Hebalkar, N.Y.; Kim, H.G.; Borse, P.H. Stabilizing effect in nano-titania functionalized CdS photoanode for sustained hydrogen generation. *Int. J. Hydrogen Energy* **2014**, *39*, 4170–4180. [[CrossRef](#)]
165. Pareek, A.; Paik, P.; Borse, P.H. Nanoniobia Modification of CdS Photoanode for an Efficient and Stable Photoelectrochemical Cell. *Langmuir* **2014**, *30*, 15540–15549. [[CrossRef](#)] [[PubMed](#)]
166. Han, S.C.; Pu, Y.C.; Zheng, L.X.; Hu, L.F.; Zhang, J.Z.; Fang, X.S. Uniform carbon-coated CdS core-shell nanostructures: Synthesis, ultrafast charge carrier dynamics, and photoelectrochemical water splitting. *J. Mater. Chem. A* **2016**, *4*, 1078–1086. [[CrossRef](#)]
167. Zhao, K.; Yan, X.Q.; Gu, Y.S.; Kang, Z.; Bai, Z.M.; Cao, S.Y.; Liu, Y.C.; Zhang, X.H.; Zhang, Y. Self-Powered Photoelectrochemical Biosensor Based on CdS/RGO/ZnO Nanowire Array Heterostructure. *Small* **2016**, *12*, 245–251. [[CrossRef](#)] [[PubMed](#)]
168. Wang, G.M.; Yang, X.Y.; Qian, F.; Zhang, J.Z.; Li, Y. Double-Sided CdS and CdSe Quantum Dot Co-Sensitized ZnO Nanowire Arrays for Photoelectrochemical Hydrogen Generation. *Nano Lett.* **2010**, *10*, 1088–1092. [[CrossRef](#)] [[PubMed](#)]
169. Bu, Y.Y.; Chen, Z.Y.; Li, W.B.; Yu, J.Q. High-efficiency photoelectrochemical properties by a highly crystalline CdS-sensitized ZnO nanorod array. *ACS Appl. Mater. Interfaces* **2013**, *5*, 5097–5104. [[CrossRef](#)] [[PubMed](#)]
170. Yuan, Y.B.; Xiao, Z.G.; Yang, B.; Huang, J.S. Arising applications of ferroelectric materials in photovoltaic devices. *J. Mater. Chem. A* **2014**, *2*, 6027–6041. [[CrossRef](#)]
171. Wei, R.B.; Kuang, P.Y.; Cheng, H.; Chen, Y.B.; Long, J.Y.; Zhang, M.Y.; Liu, Z.Q. Plasmon-Enhanced Photoelectrochemical Water Splitting on Gold Nanoparticle Decorated ZnO/CdS Nanotube Arrays. *ACS Sustain. Chem. Eng.* **2017**, *5*, 4249–4257. [[CrossRef](#)]
172. Guo, X.; Zhu, J.J.; Wei, H.X.; Lee, S.T.; Li, Y.Q.; Tang, J.X. Facile approaching hierarchical CdS films as electrode toward photoelectrochemical water splitting. *Nanotechnology* **2015**, *26*, 1–9. [[CrossRef](#)] [[PubMed](#)]
173. Zhang, Z.M.; Gao, C.T.; Wu, Z.M.; Han, W.H.; Wang, Y.L.; Fu, W.B.; Li, X.D.; Xie, E.Q. Toward efficient photoelectrochemical water-splitting by using screw-like SnO₂ nanostructures as photoanode after being decorated with CdS quantum dots. *Nano Energy* **2016**, *19*, 318–327. [[CrossRef](#)]
174. Tran, T.K.; Park, W.; Tong, W.; Kyi, M.M.; Wagner, B.K.; Summers, C.J. Photoluminescence properties of ZnS epilayers. *J. Appl. Phys.* **1997**, *81*, 2803–2809. [[CrossRef](#)]
175. Zhang, J.; Yu, J.G.; Jaroniec, M.; Gong, J.R. Noble Metal-Free Reduced Graphene Oxide-Zn_xCd_{1-x}S Nanocomposite with Enhanced Solar Photocatalytic H₂-Production Performance. *Nano Lett.* **2012**, *12*, 4584–4589. [[CrossRef](#)] [[PubMed](#)]
176. Hong, Y.P.; Zhang, J.; Wang, X.; Wang, Y.J.; Lin, Z.; Yu, J.G.; Huang, F. Influence of lattice integrity and phase composition on the photocatalytic hydrogen production efficiency of ZnS nanomaterials. *Nanoscale* **2012**, *4*, 2859–2862. [[CrossRef](#)] [[PubMed](#)]
177. Meier, J.H.; Meier, K. Photochemical production of hydrogen with Zinc Sulfide suspensions. *J. Phys. Chem.* **1984**, *88*, 5903–5913.
178. Hu, J.S.; Ren, L.L.; Guo, Y.G.; Liang, H.P.; Cao, A.M.; Wan, L.J.; Bai, C.L. Mass Production and High Photocatalytic Activity of ZnS Nanoporous Nanoparticles. *Angew. Chem. Int. Ed.* **2005**, *44*, 1269–1273. [[CrossRef](#)] [[PubMed](#)]
179. Youn, H.C.; Barral, S.; Fendler, J.H. Dihexadecyl Phosphate, Vesicle-Stabilized and in Situ Generated Mixed CdS and ZnS Semiconductor Particles. Preparation and Utilization for Photosensitized Charge Separation and Hydrogen Generation. *J. Phys. Chem.* **1988**, *92*, 6320–6327. [[CrossRef](#)]
180. Kudo, A.; Sekizawa, M. Photocatalytic H₂ evolution under visible light irradiation on Zn_{1-x}Cu_xS solid solution. *Catal. Lett.* **1999**, *58*, 241–243. [[CrossRef](#)]
181. Kudo, A.; Sekizawa, M. Photocatalytic H₂ evolution under visible light irradiation on Ni-doped ZnS photocatalyst. *Chem. Commun.* **2000**, *0*, 1371–1372. [[CrossRef](#)]
182. Hassan, M.A.; Kang, J.H.; Johar, M.A.; Ha, J.S.; Ryu, S.W. High-performance ZnS/GaN heterostructure photoanode for photoelectrochemical water splitting applications. *Acta Mater.* **2018**, *146*, 171–175. [[CrossRef](#)]
183. Herrmann, J.M.; Disdier, J.; Pichat, P. Effect of chromium doping on the electrical and catalytic properties of powder titania under UV and visible illumination. *Chem. Phys. Lett.* **1984**, *108*, 618–622. [[CrossRef](#)]

184. Kaneva, N.V.; Dimitrov, D.T.; Dushkin, C.D. Effect of nickel doping on the photocatalytic activity of ZnO thin films under UV and visible light. *Appl. Surf. Sci.* **2011**, *257*, 8113–8120. [[CrossRef](#)]
185. Bellam, J.B.; Ruiz-Preciado, M.A.; Edely, M.; Szade, J.; Jouanneaux, A.; Kassiba, A.H. Visible-light photocatalytic activity of nitrogen-doped NiTiO₃ thin films prepared by a co-sputtering process. *RSC Adv.* **2015**, *5*, 10551–10559. [[CrossRef](#)]
186. Hajjaji, A.; Trabelsi, K.; Atyaoui, A.; Gaidi, M.; Bousselmi, L.; Bessais, B.; El Khakani, M.A. Photocatalytic activity of Cr-doped TiO₂ nanoparticles deposited on porous multicrystalline silicon films. *Nanoscale Res. Lett.* **2014**, *9*, 1–6. [[CrossRef](#)] [[PubMed](#)]
187. Kurnia, F.; Ng, Y.H.; Amal, R.; Valanoor, N.; Hart, J.N. Defect engineering of ZnS thin films for photoelectrochemical water-splitting under visible light. *Sol. Energy Mater. Sol. Cells C* **2016**, *153*, 179–185. [[CrossRef](#)]
188. Rai, S.C.; Wang, K.; Ding, Y.; Marmon, J.K.; Bhatt, M.; Zhang, Y.; Zhou, W.L.; Wang, Z.L. Piezo-phototronic Effect Enhanced UV/Visible Photodetector Based on Fully Wide Band Gap Type-II ZnO/ZnS Core/Shell Nanowire Array. *ACS Nano* **2015**, *9*, 6419–6427. [[CrossRef](#)] [[PubMed](#)]
189. Liu, C.H.; Qiu, Y.Y.; Wang, F.; Li, L.Z.; Liang, Q.; Chen, Z.D. Electrodeposition of ZnO nanoflake-based photoanode sensitized by carbon quantum dots for photoelectrochemical water oxidation. *Ceram. Int.* **2017**, *43*, 5329–5333. [[CrossRef](#)]
190. Tian, W.; Zhang, C.; Zhai, T.; Li, S.L.; Wang, X.; Liu, J.W.; Jie, X.; Liu, D.Q.; Liao, M.Y.; Koide, Y.S.; et al. Flexible Ultraviolet Photodetectors with Broad Photoresponse Based on Branched ZnS-ZnO Heterostructure Nanofilms. *Adv. Mater.* **2014**, *26*, 3088–3093. [[CrossRef](#)] [[PubMed](#)]
191. Wang, M.D.; Chen, C.X.; Qin, H.Y.; Zhang, L.; Fang, Y.T.; Liu, J.B.; Meng, L. Construction of FeS₂-Sensitized ZnO@ZnS Nanorod Arrays with Enhanced Optical and Photoresponse Performances. *Adv. Mater. Interfaces* **2015**, *2*, 1–10. [[CrossRef](#)]
192. Tian, W.; Zhai, T.Y.; Zhang, C.; Li, S.L.; Wang, X.; Liu, F.; Liu, D.Q.; Cai, X.K.; Tsukagoshi, K.; Golberg, D.; et al. Low-Cost Fully Transparent Ultraviolet Photodetectors Based on Electrospun ZnO-SnO₂ Heterojunction Nanofibers. *Adv. Mater.* **2013**, *25*, 4625–4630. [[CrossRef](#)] [[PubMed](#)]
193. Kushwaha, A.; Aslam, M. ZnS shielded ZnO nanowire photoanodes for efficient water splitting. *Electrochim. Acta* **2014**, *130*, 222–231. [[CrossRef](#)]
194. Wu, X.; Jiang, P.; Ding, Y.; Cai, W.; Xie, S.; Wang, Z.L. Mismatch strain induced formation of ZnO/ZnS heterostructured rings. *Adv. Mater.* **2007**, *19*, 2319–2323. [[CrossRef](#)]
195. Sánchez-Tovar, R.; Fernández-Domene, R.M.; Montañés, M.T.; Sanz-Marco, A.; Garcia-Antón, J. ZnO/ZnS heterostructures for hydrogen production by photoelectrochemical water splitting. *RSC Adv.* **2016**, *6*, 30425–30435. [[CrossRef](#)]
196. Liu, Y.C.; Gu, Y.S.; Yan, X.Q.; Kang, Z.; Lu, S.N.; Sun, Y.H.; Zhang, Y. Design of sandwich-structured ZnO/ZnS/Au photoanode for enhanced efficiency of photoelectrochemical water splitting. *Nano Res.* **2015**, *8*, 2891–2900. [[CrossRef](#)]
197. Liu, C.H.; Qiu, Y.Y.; Wang, F.; Wang, K.; Liang, Q.; Chen, Z.D. Design of Core-Shell-Structured ZnO/ZnS Hybridized with Graphite-Like C₃N₄ for Highly Efficient Photoelectrochemical Water Splitting. *Adv. Mater. Interfaces* **2017**, *4*, 1–11. [[CrossRef](#)]
198. Huang, J.D.; Liu, J.Y.; Han, K.L. Hybrid functionals studies of structural and electronic properties of Zn_xCd_(1-x)S and (Zn_xCd_{1-x})(SexS_{1-x}) solid solution photocatalysts. *Int. J. Hydrogen Energy* **2012**, *37*, 17870–17881. [[CrossRef](#)]
199. Jang, G.G.; Jacobs, C.B.; Ivanov, I.N.; Joshi, P.C.; Iii, H.M.M.; Kidder, M.; Armstrong, B.L.; Datskos, P.G.; Graham, D.E.; Moon, J.W. In situ capping for size control of monochalcogenide (ZnS, CdS and SnS) nanocrystals produced by anaerobic metal-reducing bacteria. *Nanotechnology* **2015**, *26*, 1–5. [[CrossRef](#)] [[PubMed](#)]
200. Qutub, N.; Pirzada, B.M.; Umar, K.; Mehraj, O.; Muneer, M.; Sabir, S. Synthesis, characterization and visible-light driven photocatalysis by differently structured CdS/ZnS sandwich and core-shell nanocomposites. *Physica E* **2015**, *74*, 74–86. [[CrossRef](#)]
201. Xu, J.Y. Preparation of ZnS-CdS nanocomposite for photoelectrochemical hydrogen production. *Int. J. Electrochem. Sci.* **2017**, *12*, 2253–2261. [[CrossRef](#)]
202. Zhang, P.; Guan, B.Y.; Yu, L.; Lou, X.W. Facile Synthesis of Multi-shelled ZnS-CdS Cages with Enhanced Photoelectrochemical Performance for Solar Energy Conversion. *CHEM* **2018**, *4*, 162–173. [[CrossRef](#)]

203. Im, J.H.; Jang, I.H.; Pellet, N.; Gratzel, M.; Park, N.G. Growth of $\text{CH}_3\text{NH}_3\text{PbI}_3$ cuboids with controlled size for high-efficiency perovskite solar cells. *Nat. Nanotechnol.* **2014**, *9*, 927–932. [[CrossRef](#)] [[PubMed](#)]
204. Burschka, J.; Pellet, N.; Moon, S.J.; Humphry-Baker, R.; Gao, P.; Nazeeruddin, M.K.; Gratzel, M. Sequential deposition as a route to high-performance perovskite-sensitized solar cells. *Nature* **2013**, *499*, 316–320. [[CrossRef](#)] [[PubMed](#)]
205. Mei, A.; Li, X.; Liu, L.F.; Ku, Z.L.; Liu, T.F.; Rong, Y.G.; Xu, M.; Hu, M.; Chen, J.Z.; Yang, Y.; et al. A hole-conductor-free, fully printable mesoscopic perovskite solar cell with high stability. *Science* **2014**, *345*, 295–298. [[CrossRef](#)] [[PubMed](#)]
206. Li, L.; Shi, C.W.; Deng, X.L.; Wang, Y.Q.; Ni, L.L. High-crystallinity and large-grain $\text{CH}_3\text{NH}_3\text{PbI}_3$ thin films for efficient TiO_2 nanorod. *IET Micro Nano Lett.* **2018**, *13*, 131–134. [[CrossRef](#)]
207. Dong, Q.F.; Fang, Y.J.; Shao, Y.C.; Mulligan, P.; Qiu, J.; Cao, L.; Huang, J.S. Electron-hole diffusion lengths > 175 μm in solution-grown $\text{CH}_3\text{NH}_3\text{PbI}_3$ single crystals. *Science* **2015**, *347*, 967–970. [[CrossRef](#)] [[PubMed](#)]
208. NREL. Available online: <https://www.nrel.gov/pv/assets/images/efficiency-chart.png>2016 (accessed on 4 July 2017).
209. Frost, J.M.; Butler, K.T.; Brivio, F.; Hendon, C.H.; van Schilfhaarde, M.; Walsh, A. Atomistic Origins of High-Performance in Hybrid Halide Perovskite Solar Cells. *Nano Lett.* **2014**, *14*, 2584–2590. [[CrossRef](#)] [[PubMed](#)]
210. Baikie, T.; Fang, Y.N.; Kadro, J.M.; Schreyer, M.; Wei, F.X.; Mhaisalkar, S.G.; Graetzel, M.; White, T.J. Synthesis and crystal chemistry of the hybrid perovskite $(\text{CH}_3\text{NH}_3)\text{PbI}_3$ for solid-state sensitised solar cell applications. *J. Mater. Chem. A* **2013**, *1*, 5628–5641. [[CrossRef](#)]
211. Luo, J.S.; Im, J.H.; Mayer, M.T.; Schreier, M.; Nazeeruddin, M.K.; Park, N.G.; Tilley, S.D.; Fan, H.J.; Gratzel, M. Water photolysis at 12.3% efficiency via perovskite photovoltaics and Earth-abundant catalysts. *Science* **2014**, *345*, 1593–1596. [[CrossRef](#)] [[PubMed](#)]
212. Da, P.M.; Cha, M.Y.; Sun, L.; Wu, Y.Z.; Wang, Z.S.; Zheng, G.F. High-performance perovskite photoanode enabled by Ni passivation and catalysis. *Nano Lett.* **2015**, *15*, 3452–3457. [[CrossRef](#)] [[PubMed](#)]



© 2018 by the authors. Licensee MDPI, Basel, Switzerland. This article is an open access article distributed under the terms and conditions of the Creative Commons Attribution (CC BY) license (<http://creativecommons.org/licenses/by/4.0/>).